



# Novel function of ceramide for regulation of mitochondrial ATP release in astrocytes<sup>S</sup>

Ji-Na Kong,<sup>1,\*†</sup> Zhihui Zhu,<sup>1,\*§</sup> Yutaka Itokazu,<sup>\*</sup> Guanghu Wang,<sup>\*\*§</sup> Michael B. Dinkins,<sup>\*</sup> Liansheng Zhong,<sup>\*,§,\*\*</sup> Hsuan-Pei Lin,<sup>\*,§</sup> Ahmed Elsherbini,<sup>\*,§</sup> Silvia Leanhart,<sup>\*</sup> Xue Jiang,<sup>§,††</sup> Haiyan Qin,<sup>§</sup> Wenbo Zhi,<sup>§§</sup> Stefka D. Spassieva,<sup>2,§</sup> and Erhard Bieberich<sup>2,\*§</sup>

Department of Neuroscience and Regenerative Medicine\* and Center of Biotechnology and Genomic Medicine,<sup>§§</sup> Medical College of Georgia, Augusta University, Augusta, GA; Department of Biology,<sup>†</sup> Massachusetts Institute of Technology, Cambridge, MA; Department of Physiology,<sup>§</sup> University of Kentucky, Lexington, KY; College of Basic Medicine,<sup>\*\*</sup> China Medical University, Shenyang, People's Republic of China; and Rehabilitation Center,<sup>††</sup> ShengJing Hospital of China Medical University, Shenyang, People's Republic of China

**Abstract** We reported that amyloid  $\beta$  peptide ( $A\beta_{42}$ ) activated neutral SMase 2 (nSMase2), thereby increasing the concentration of the sphingolipid ceramide in astrocytes. Here, we show that  $A\beta_{42}$  induced mitochondrial fragmentation in wild-type astrocytes, but not in nSMase2-deficient cells or astrocytes treated with fumonisin B1 (FB1), an inhibitor of ceramide synthases. Unexpectedly, ceramide depletion was concurrent with rapid movements of mitochondria, indicating an unknown function of ceramide for mitochondria. Using immunocytochemistry and super-resolution microscopy, we detected ceramide-enriched and mitochondria-associated membranes (CEMAMs) that were codistributed with microtubules. Interaction of ceramide with tubulin was confirmed by cross-linking to *N*-[9-(3-pent-4-ynyl-3-H-diazirine-3-yl)-nonanoyl]-D-erythro-sphingosine (pacFACer), a bifunctional ceramide analog, and binding of tubulin to ceramide-linked agarose beads. Ceramide-associated tubulin (CAT) translocated from the perinuclear region to peripheral CEMAMs and mitochondria, which was prevented in nSMase2-deficient or FB1-treated astrocytes. Proximity ligation and coimmunoprecipitation assays showed that ceramide depletion reduced association of tubulin with voltage-dependent anion channel 1 (VDAC1), an interaction known to block mitochondrial ADP/ATP transport. Ceramide-depleted astrocytes contained higher levels of ATP, suggesting that ceramide-induced CAT formation leads to VDAC1 closure, thereby reducing mitochondrial ATP release, and potentially motility and resistance to  $A\beta_{42}$ .<sup>¶¶</sup> Our data also indicate that inhibiting ceramide generation may protect mitochondria in Alzheimer's disease.—Kong, J-N., Z. Zhu, Y. Itokazu, G. Wang, M. B. Dinkins, L. Zhong, H-P. Lin, A. Elsherbini, S. Leanhart, X. Jiang, H. Qin, W. Zhi, S. D. Spassieva, and E. Bieberich. **Novel function of ceramide for**

**regulation of mitochondrial ATP release in astrocytes.** *J. Lipid Res.* 2018. 59: 488–506.

**Supplementary key words** adenosine 5'-triphosphate • sphingolipids • mitochondria-associated membranes

In addition to accumulating amyloid  $\beta$  peptide ( $A\beta_{42}$ ), elevation of ceramide and mitochondrial damage is observed in Alzheimer's disease (AD) (1, 2). Our laboratory discovered that incubation of astrocytes with  $A\beta_{42}$  activates neutral SMase 2 (nSMase2), a bona fide signaling enzyme generating ceramide from sphingomyelin (3, 4). While examining the effect of  $A\beta_{42}$  on astrocytes in time-lapse imaging, we discovered that mitochondria in nSMase2-deficient astrocytes were more resistant to  $A\beta_{42}$ -induced damage, but they also moved more rapidly than those in wild-type astrocytes. nSMase2 has been shown to shuttle between the plasma membrane and Golgi and it is activated by mitochondrial lipids (5–8), prompting us to test the effect of nSMase2-generated ceramide on mitochondrial motility and function.

Ceramide is a sphingolipid the concentration of which is less than 1 mol% (compared with approximately 10 mol%

Abbreviations: ACN, acetonitrile; AD, Alzheimer's disease;  $A\beta_{42}$ , amyloid  $\beta$  peptide; CAT, ceramide-associated tubulin; CEC, ceramide-enriched compartment; CerS, ceramide synthase; CEMAM, ceramide-enriched and mitochondria-associated membrane; dSTORM, direct stochastic optical reconstruction microscopy; ER, endoplasmic reticulum; FB1, fumonisin B1; MAM, mitochondria-associated membrane; nSMase2, neutral SMase 2; NSTORM, Nikon STORM OMM, outer mitochondrial membrane; pacFACer, *N*-[9-(3-pent-4-ynyl-3-H-diazirine-3-yl)-nonanoyl]-D-erythro-sphingosine; PLA, proximity ligation assay; SigmaR1, sigma 1 receptor; STORM, stochastic optical reconstruction microscopy; VDAC1, voltage-dependent anion channel 1.

<sup>1</sup>J-N. Kong and Z. Zhu contributed equally to this work.

<sup>2</sup>To whom correspondence should be addressed.

e-mail: erhard.bieberich@uky.edu (E.B.);

stefanka.spassieva@uky.edu (S.D.S.)

<sup>S</sup> The online version of this article (available at <http://www.jlr.org>) contains a supplement.

This work was supported by National Institute on Aging Grant R01AG034389, National Institute of Neurological Disorders and Stroke Grant R01NS095215, the National Science Foundation, and Division of Molecular and Cellular Biosciences Grant 1615874. The content is solely the responsibility of the authors and does not necessarily represent the official views of the National Institutes of Health.

Manuscript received 15 November 2017 and in revised form 8 January 2018.

Published, *JLR Papers in Press*, January 10, 2018

DOI <https://doi.org/10.1194/jlr.M081877>

Copyright © 2018 by the American Society for Biochemistry and Molecular Biology, Inc.

This article is available online at <http://www.jlr.org>

sphingomyelin) in cellular membranes (9). It is mainly synthesized in the endoplasmic reticulum (ER) by ceramide synthases (CerSs), which attach a variety of fatty acid residues to long chain bases, such as sphingosine and dihydro-sphingosine, or by hydrolysis of sphingomyelin that is catalyzed by different SMases in distinct cellular compartments, such as the plasma membrane, lysosomes, the Golgi apparatus, and mitochondria (10–15). Increase of ceramide levels through upregulation of CerSs or SMases leads to induction of apoptosis and other cell signaling pathways critical for cell death, senescence, autophagy, or cell cycle arrest. We and others showed that the localized generation or distribution of ceramide in ceramide microdomains (rafts) or more extended ceramide-enriched compartments (CECs) may have additional cellular functions of ceramide (16–23). Instrumental to our studies was the generation of a ceramide-specific antibody originally developed in our laboratory (24). This antibody has been shared with several independent laboratories to reliably detect and visualize ceramide in cells and tissues and it is the only antibody applicable to super-resolution microscopy using stochastic optical reconstruction microscopy (STORM) (3, 18, 25–27). In addition to the ceramide-specific antibody, we developed a novel imaging protocol based on cross-linking of photoactivatable ceramide analogs [bifunctional ceramide or *N*-[9-(3-pent-4-ynyl-3-H-diazirine-3-yl)-nonanoyl]-D-erythro-sphingosine (pacFACer)] that can be derivatized with fluorophores or biotin using click chemistry. We demonstrated that these ceramide analogs are distributed to CECs and can be used to visualize and identify proteins binding to ceramide (19).

Previous studies showed that ceramide analogs were cross-linked or bound to tubulin (28, 29). We showed that tubulin was coimmunoprecipitated when pulling down intracellular vesicles using anti-ceramide IgG (20). These studies suggested that ceramide may bind to free tubulin dispersed in the cytosol, or to tubulin embedded into microtubules or associated with cellular membranes (membrane tubulin). Membrane tubulin has been detected in the plasma membrane, but also in other compartments and organelles, such as the ER and mitochondria (30, 31). Tubulin has been suggested to bind to lipids in the cytosolic leaflet of the outer mitochondrial membrane (OMM) to initiate closure of voltage-dependent anion channel 1 (VDAC1) (32–34), one of the key channels mediating ADP/ATP transport between mitochondria and the cytosol.

Malfunction of mitochondria and dysregulated VDAC1 have been implicated in many neurodegenerative diseases, including AD, Huntington's disease, Parkinson's disease, amyotrophic lateral sclerosis, and frontotemporal dementia (35–42). In AD, A $\beta$  has been shown to bind to VDAC1, reduce ATP levels, and cause mitochondrial fragmentation during early stages of the disease (35, 43, 44). VDAC1 downregulation has been reported to reduce cellular ATP levels and induce mitochondrial fragmentation (45, 46), eventually leading to neurodegeneration. In astrocytes, VDAC1 is critical for secretion of ATP, a gliotransmitter regulating synaptic plasticity and neuronal function (47–50). Most recently, VDAC1 closure by tubulin has been suggested

to be critical for the Warburg effect, a metabolic switch from mitochondria-mediated oxidative phosphorylation to glycolysis for ATP production, often observed in cancer cells (51–53).

While assays with mitochondria showed that lipid-tubulin interaction is important for tubulin-mediated VDAC1 closure (52, 54–56), the role of ceramide in this regulation has not been investigated yet. In addition, there is only little information available on the role of lipid-tubulin interaction for the function of mitochondria in intact cells. Studies from several laboratories found that ceramide is enriched in mitochondria and mitochondria-associated membranes (MAMs) (57, 58). MAMs are a subcompartment of the ER that forms contact sites with mitochondria and takes part in the cross-talk between mitochondria and microtubules. While CerSs and nSMases have been shown to generate ceramide in mitochondria involved in inducing apoptosis (59–62), it is not known whether ceramide regulates the function of MAMs and whether this involves ceramide-associated tubulin (CAT) and its effect on VDAC1.

To test a potential role of CAT located at MAMs for the regulation of mitochondria, we used several complementary experimental approaches: 1) determining the effect of ceramide depletion by nSMase2 deficiency or the CerS inhibitor, fumonisin B1 (FB1), on mitochondrial morphology and motility; 2) confocal microscopy and STORM using anti-ceramide IgG for testing the association of ceramide with mitochondria and microtubules; 3) cross-linking of pacFACer and binding to ceramide agarose beads to test ceramide association to tubulin; 4) proximity ligation assays (PLAs) and coimmunoprecipitation assays to quantify CAT and CAT-VDAC1 complexes in primary cultured astrocytes and test the effect of ceramide depletion on complex formation; and 5) measurement of ATP levels in nSMase2-deficient or FB1-treated astrocytes to determine the effect of ceramide depletion on CAT-induced VDAC1 closure. Our results suggest that CAT localized at ceramide-enriched MAMs (CEMAMs) induces interaction of tubulin with VDAC1, a novel regulatory mechanism critical for mitochondria and, potentially, pathophysiology in AD.

## MATERIALS AND METHODS

### Reagents

MitoTracker Red CM-H<sub>2</sub>Xros (M-7513), Duolink PLA probe anti-rabbit plus (DUO92002), Duolink PLA probe anti-mouse minus (DUO92004), Duolink PLA probe anti-goat minus (DUO92006), Duolink detection reagent red (DUO92008), Duolink detection reagent green (DUO92014), Alexa Fluor 647 azide (A10277), Invitrogen Click-iT cell reaction buffer kit (C10269), and Click-iT protein reaction buffer kit (C10276) were purchased from Thermo Fisher Scientific (West Columbia, SC); CytoPainter mitochondrial staining kit-green fluorescence (ab112143) and ATP photometric/fluorimetric assay (ab83355) were from Abcam (Cambridge, MA); pacFACer was obtained from Avanti Polar Lipids (Alabaster, AL); TAMRA-azide-desthiobiotin (1110-5) was from

Click Chemistry Tools (Scottsdale, AZ); cyanine 7.5 azide (A6030) was purchased from Lumiprobe (Hallandale Beach, FL); 2-mercaptoethanol (636890), cysteamine (30070), glucose oxidase from *Aspergillus niger* type VII (G2133-250 KU), and catalase from bovine liver (C40) were purchased from Sigma-Aldrich (St. Louis, MO). A $\beta$ <sub>1-42</sub> was from Anaspec (Freemont, CA) dissolved in 1% ammonia and diluted to 1 mg/ml and neutralized in PBS prior to use.

### Preparation and treatment of primary astrocytes cultures

All experiments were carried out according to an Animal Use Protocol approved by the Institutional Animal Care and Use Committee at Augusta University and the University of Kentucky. Primary glial cells were isolated from brains of P0-P1 (day at birth or next day) C57BL/6 wild-type or nMase2-deficient *fro/fro* mouse pups. Brains were dissociated in PBS containing 0.1 M glucose, passed through a 40  $\mu$ m filter, and plated in T-25 flasks in DMEM (Life Technologies, Grand Island, NY) supplemented with 10% fetal bovine serum, and 1% penicillin/streptomycin solution at 37°C in a humidified atmosphere containing 5% CO<sub>2</sub>. After 7 days, adherent cells were passed to 24-well plates containing uncoated glass coverslips and cultured in DMEM as described above.

### Immunocytochemistry and confocal microscopy

Cells were fixed with 4% p-formaldehyde/0.5% glutaraldehyde/PBS for 15 min and then permeabilized by incubation with 0.2% Triton X-100 in PBS for 5 min at room temperature. Non-specific binding sites were blocked with 3% ovalbumin/PBS for 1 h at 37°C. The primary antibodies used were: anti-acetylated tubulin mouse IgG (1:3,000, Sigma-Aldrich, clone 6-1113-1, T6793), anti-ceramide rabbit IgG (1:100, our laboratory) (20, 24), anti-ceramide mouse IgM (1:100, MAB0014, Glycobiotech GmbH), anti-sigma receptor 1 goat IgG (1:200, Santa Cruz, clone S-18, sc-22948), anti- $\alpha$ -tubulin mouse monoclonal IgG (1:200, Santa Cruz, clone B-7, sc-5286), anti- $\beta$ -tubulin goat IgG (1:200, Santa Cruz, clone N-20, sc-9935), anti- $\beta$ -tubulin mouse monoclonal IgG (1:200, Santa Cruz, clone D-10, sc-5274), anti-calnexin goat IgG (1:200, Santa Cruz, sc-6465), anti-Tom 20 rabbit IgG (1:200, Santa Cruz, sc-11415), anti-tubb4 mouse IgG (1:200, Invitrogen, 1-20247), anti-IP3 receptor mouse IgG (1:200, University of California Davis/National Institutes of Health NeuroMab facility, clone L2418), anti-VDAC1 rabbit IgG (1:500, Abcam, ab15895). Secondary antibodies (Alexa Fluor 546-conjugated donkey anti-rabbit IgG, Cy5-conjugated donkey anti-mouse IgM  $\mu$ -chain specific, Alexa Fluor 647-conjugated goat anti-mouse IgG  $\gamma$ -chain specific (all Jackson ImmunoResearch, West Grove, PA) were diluted 1:300 in 0.1% ovalbumin/PBS and samples incubated for 2 h at 37°C. After washing, coverslips were mounted using Fluoro-shield supplemented with DAPI (Sigma-Aldrich) to visualize the nuclei. Confocal fluorescence microscopy was performed using a Zeiss LSM780 upright confocal laser scanning microscope (Zeiss, Jena, Germany) equipped with a two-photon argon laser at 488, 543, or 633 nm. Images were processed using Zeiss Zen software.

### Image analysis of colocalization and motility

Randomly chosen sections of images (blinded) were analyzed using the colocalization 2 function in Fiji/Image J software. The degree of colocalization was assessed by calculation of the Pearson's correlation coefficient for two fluorescence channels in overlays, as previously described (63). A similar technique was used for determining motility of mitochondria using overlays of two consecutive time frames assigned to two different fluorescence channels. Motility was inversely correlated to the Pearson's correlation coefficient in the overlay. All of the data were collected from three independent cell cultures using five randomly selected areas per culture for determination of mitochondrial motility.

### NSTORM

Cells were fixed and subjected to immunocytochemistry using primary antibodies, as described for confocal microscopy. To ensure the optical properties required for STORM, Atto 488 anti-rabbit and Alexa Fluor 647 anti-mouse antibodies were used as secondary antibodies. Samples were immersed in buffers prepared as follows: buffer A, 10 mM Tris (pH 8.0) + 50 mM NaCl; buffer B, 50 mM Tris (pH 8.0) + 10 mM NaCl + 10% glucose; GLOX solution (250  $\mu$ l), 14 mg glucose oxidase (Sigma-Aldrich) + 50  $\mu$ l catalase from bovine liver-lyophilized powder (17 mg/ml) (Sigma-Aldrich) + 200  $\mu$ l buffer A. Buffers A and B were freshly prepared, vortexed, and spun down at 13,000 rpm. Only the supernatant was used for preparing the NSTORM imaging buffer by adding 7  $\mu$ l GLOX and 70  $\mu$ l 1 M cysteamine (MEA) (Sigma-Aldrich) to 620  $\mu$ l buffer B in a 1.5 ml Eppendorf tube on ice, followed by gently mixing and adding the buffer to the sample for imaging. NSTORM was performed using a Nikon Storm microscope equipped with 405, 488, 561, and 633 nm lasers and proprietary software for image reconstruction.

### Cross-linking to pacFACer and click chemistry-mediated tagging with fluorophores

Astrocytes were incubated under protection from light for 5–60 min in DMEM medium with vehicle (1:1,000 ethanol/2% dodecane) or 5  $\mu$ M of the bifunctional ceramide analog, pacFACer (Avanti Polar Lipids) diluted 1:1,000 from a stock in ethanol/2% dodecane. Cells were UV irradiated at 365 nm for 15 min at room temperature and fixed with 4% p-formaldehyde/0.5% glutaraldehyde/PBS for 15 min. Unbound pacFACer was removed by washing and fixing with ice-cold methanol for 15 min. For immunocytochemistry, cells were washed with PBS, equilibrated with click reaction buffer, and the click reaction performed using the Click-iT cell reaction buffer kit using Alexa Fluor 594-azide or TAMRA-azide-biotin as fluorophores following the manufacturer's protocol (Life Technologies).

### pacFACer cross-linking and streptavidin pull-down

Homogenates of primary cultured astrocytes were incubated with pacFACer (10  $\mu$ M) for 30 min at room temperature. The homogenate was UV irradiated at 365 nm for 20 min. Unbound pacFACer was removed by chloroform/methanol precipitation. Protein precipitates were dissolved with 1% SDS in 50 mM Tris-HCl buffer (pH 7.5) and sonicated. The click reaction was performed using the Click-iT protein reaction buffer kit (Thermo Fisher Scientific) with 500  $\mu$ M of biotin azide (Sigma-Aldrich) following the manufacturer's protocol. Unbound biotin azide was removed by chloroform/methanol precipitation. The resulting protein pellets were dissolved in 1% SDS in 50 mM Tris-HCl buffer (pH 7.5), diluted to 0.1% SDS for pull-down experiment. The insoluble materials were removed by centrifugation at 20,000 g for 5 min at room temperature. Supernatants equivalent to the same amount of protein were incubated with 25  $\mu$ l of preequilibrated NeutrAvidin beads (Thermo Fisher Scientific) for 2 h at room temperature. Beads were washed 10 times with 0.1% SDS in 50 mM Tris-HCl buffer (pH 7.5). For immunoblotting, pacFACer-binding proteins were eluted with SDS-sample buffer containing 10% 2-mercaptoethanol for 30 min at 60°C.

### Affinity purification using ceramide beads

Ceramide-coated beads (P-BCer, Echelon Bioscience) and control beads (P-B000, Echelon Bioscience) were incubated with an equal amount of astrocyte lysates. In detail, primary cultured astrocytes were harvested in ceramide binding buffer [20 mM Tris-HCl, 150 mM NaCl, and 1 mM EDTA (pH 7.5) supplemented

with protein inhibitor cocktail (Roche)]. The cells were homogenized by glass homogenizer on ice, and complete lysis of cells was achieved by sonication. After insoluble debris was removed by centrifugation at 20,800 *g* for 30 min at 4°C, Triton X-100 was added to the supernatant at 0.25% of final concentration. A 20  $\mu$ l slurry of ceramide beads and control beads was added to the supernatant and incubated at 4°C overnight under rotary agitation. Beads were harvested by centrifugation at 4°C, 500 *g* for 5 min and washed four times with ceramide binding buffer supplemented with 0.25% Triton X-100. The bound proteins were eluted by SDS-sample buffer containing 10% 2-mercaptoethanol for 30 min at 60°C and then subjected to SDS-PAGE either for immunoblotting or Coomassie staining. Stained bands were cut out and subjected to proteomics analysis.

#### pacFACer ELISA and cross-linking to recombinant tubulin

Binding assays were performed using pacFACer lipid ELISA as described previously (19, 20, 24). Briefly, pacFACer (500 ng in 100  $\mu$ l ethanol) was coated on 96-well Immulon-1B ELISA plates (Thermo Fisher Scientific/Life Technologies) and washed with PBS. Nonspecific binding sites were blocked by incubation for 1 h at 37°C with 100  $\mu$ l of 1% BSA in PBS. Tubulin purified from pig brain (80 ng/ $\mu$ l, T240-T240-A; Cytoskeleton, Denver, CO) in PBS was incubated for 1 h at 37°C. Wells were UV irradiated at 365 nm for 15 min at room temperature. Unbound tubulin was removed by washing four times with PBS and then the click reaction performed using the Click-iT cell reaction buffer kit with Cy7.5-azide as fluorophore following the manufacturer's protocol (Life Technologies). Click chemistry reagent was removed and the wells were washed four times with PBS. SDS sample buffer was added into the wells to collect protein samples.

#### Protein identification

Gel bands were excised from SDS-PAGE gels, cut into 1 mm pieces, destained using 50% acetonitrile (ACN) in 25 mM ammonium bicarbonate, dried, reduced with dithiothreitol, alkylated using iodoacetamide, and digested overnight using trypsin. Peptides were extracted using 5% formic acid in 50% ACN and were dried. Peptide digests were analyzed on an Orbitrap Fusion Tribrid mass spectrometer (Thermo Fisher Scientific) coupled with an Ultimate 3000 nano-UPLC system (Thermo Fisher Scientific). Two microliters of reconstituted peptide were first trapped and washed on a Pepmap100 C18 trap (5  $\mu$ m, 0.3  $\times$  5 mm) at 20  $\mu$ l/min using 2% ACN in water (with 0.1% formic acid) for 10 min and then separated on a Pepman 100 RSLC C18 column (2.0  $\mu$ m, 75  $\mu$ m  $\times$  150 mm) using a gradient of 2–40% ACN with 0.1% formic acid over 40 min at a flow rate of 300 nl/min and a column temperature of 40°C.

Samples were analyzed by data-dependent acquisition in positive mode using an Orbitrap MS analyzer for precursor scan at 120,000 FWHM from *m/z* 300 to 1,500 and ion-trap MS analyzer for MS/MS scans at top speed mode (3 s cycle time). Collision-induced dissociation was used as fragmentation method. Raw data were processed using Proteome Discoverer (v1.4; Thermo Fisher Scientific) and submitted for SequestHT search against the UniProt database pertinent to the origin of the sample. Fixed value PSM validator algorithm was used for peptide spectrum matching validation. SequestHT search parameters were 10 ppm precursor and 0.6 Da product ion tolerance, with static carbamidomethylation (+57.021 Da).

#### PLAs and quantitative analysis

Astrocytes were grown on glass coverslips. Cells were fixed with 4% p-formaldehyde/0.5% glutaraldehyde/PBS for 15 min at 37°C and then permeabilized by incubation with 0.2% Triton

X-100 in PBS for 5 min at room temperature. Nonspecific binding sites were blocked with Duolink PLA blocking solution (Sigma-Aldrich) for 1 h at 37°C. The primary antibodies used were: anti-ceramide rabbit IgG (1:100, our laboratory) (20, 24), anti-VDAC1, and anti-tubb 4/5. Secondary PLA probes, anti-rabbit PLUS affinity-purified donkey anti-rabbit IgG (H+L), anti-goat MINUS affinity-purified donkey anti-goat IgG (H+L), and anti-mouse MINUS affinity-purified donkey anti-mouse IgG (H+L), were diluted 1:5 in 1 $\times$  antibody diluent buffer and samples incubated for 1 h at 37°C. After washing, ligation and amplification steps were performed following the manufacturer's protocol (Sigma-Aldrich). Coverslips were mounted using Fluoroshield supplemented with DAPI (Sigma-Aldrich) to visualize the nuclei. Zeiss LSM780 upright confocal microscopy was performed as described in one of the previous sections. Zen software was used for initial image acquisition and dots counted using ImageJ. Images obtained with secondary antibody only were used as negative controls representing the background intensity in a particular laser channel.

#### Isolation of mitochondria and coimmunoprecipitation assay

HEK293T cells were seeded on the 100 mm dishes with 35–40% of density, in the absence or presence of 3  $\mu$ M FB1 (116355-83-0; Cayman, Ann Arbor, MI). Sixty hours later, the untreated cells and the treated cells were harvested and washed twice with ice-cold PBS. The cell pellets were transferred into a Dounce homogenizer and lysed with 2 ml of ice-cold mitochondria extraction buffer [125 mM sucrose, 250 mM mannitol, 10 mM HEPES, 10 mM EGTA, 0.01% BSA, and protease inhibitors (pH 7.2)]. To enrich for mitochondria, the homogenate was transferred into a centrifuge tube and cell debris pelleted at 700 *g*, 4°C for 10 min. The supernatant was centrifuged once again under the same conditions and subsequently, transferred to a new ice-cold tube followed by centrifugation at 10,000 *g* for 15 min at 4°C. The mitochondrial pellet was resuspended in 1 ml of lipid binding buffer [20 mM Tris-HCl, 150 mM NaCl, 1 mM EDTA (pH 7.5), and 1% digitonin, supplemented with protein inhibitor cocktail (Roche)] and complete lysis of mitochondrial membranes was achieved by sonication. Insoluble debris was removed by centrifugation at 10,000 *g* for 15 min at 4°C. The protein concentration in the supernatants from untreated cells and treated cells was adjusted to the same concentration and the same volume. Lysates were pre-cleared with Pierce protein A/G magnetic beads (88802; Pierce Biotechnology, Rockford, IL) and then incubated overnight with nonspecific mouse IgG (control) or anti  $\alpha$ -tubulin mouse IgG at 4°C under rotational movement. The next morning, 15  $\mu$ l of Pierce protein A/G magnetic beads were added to the samples and incubated for 2 h at room temperature under rotational movement. The beads were harvested and washed three times by lipid binding buffer without digitonin. Protein bound to the beads was eluted by SDS-sample buffer containing 10% 2-mercaptoethanol for 30 min at room temperature. The protein preparation was subjected to SDS-PAGE for immunoblotting using anti-VDAC1 rabbit IgG.

#### ATP determination

Wild-type and *fro/fro* astrocytes ( $10^6$  cells) were detached using trypsin/EDTA solution and resuspended in ice-cold PBS. Total cellular ATP was determined following the fluorescence protocol as described in the manual provided by the supplier (Abcam). All measurements were performed in triplicate and normalized to cell number and protein.

#### Morphometric analysis of mitochondria

Measurement of mitochondrial length (L) and width (W), perimeter (P), and area (A) was achieved using ImageJ after correction

for contrast and background. Mitochondrial morphology was analyzed using standard protocols for quantitation of mitochondrial length (L), aspect ratio (L/W), and form factor ( $P^2/4\pi A$ ), as previously described (64).

### Statistical analysis

The mean, SEM, and statistical tests of control and treatment samples were calculated using GraphPad Prism. Student's *t*-test was used to compare two groups, one-way ANOVA with Bonferroni post hoc test for three or more groups. Values of at least  $P < 0.05$  were considered significant.

### Miscellaneous

For immunoblot analysis, protein concentrations were determined using the RC/DC protein assay, in accordance with the manufacturer's (Bio-Rad) instructions. Equal amounts of protein were loaded onto a 4–20% gradient gel, and SDS-PAGE was performed using the Laemmli method. For immunoblotting, membranes were first blocked with 5% dry milk in PBST (PBS containing 0.1% Tween-20) and incubated with primary antibodies in the blocking buffer overnight at 4°C. Membranes were then washed three times with PBS/0.05% Tween and incubated with the appropriate horseradish peroxidase-conjugated secondary antibodies for 1 h at room temperature. After washing, bands were detected using an Odyssey imaging system from Licor or Pico and Femto ECL assay from Pierce/Thermo Fisher Scientific.

## RESULTS

### Mitochondria in ceramide-depleted astrocytes are resistant to A $\beta$ -induced fragmentation and show increased motility

Our previous studies showed that incubation with A $\beta_{42}$  leads to increased levels of ceramide in primary cultured astrocytes and that nSMase2 deficiency reduces ceramide levels and sensitivity of astrocytes to A $\beta$ -induced apoptosis (supplemental Fig. S1A) (4). In addition, it has been shown that A $\beta_{42}$  induces fragmentation of mitochondria (44). Therefore, we tested to determine whether mitochondria in nSMase2-deficient astrocytes were resistant to A $\beta$ -induced fragmentation. **Figure 1A** shows that overnight exposure to 1  $\mu$ M A $\beta_{42}$  led to fragmented mitochondria in wild-type, but not in nSMase2-deficient, astrocytes (see supplemental Fig. S1B, C for controls). Fragmentation led to about 50% reduction in mitochondrial length, aspect ratio, and form factor (Fig. 1B–D), consistent with previous studies showing similar effects of amyloid on mitochondrial morphology (64). As an alternative approach to deplete cells of ceramide, we used the CerS inhibitor, FBI, which also protected astrocytes from mitochondrial fragmentation (supplemental Fig. S1A, ceramide profile; supplemental Fig. S1D, E, mitochondria). These results suggested that independent of the affected metabolic pathway (via nSMase2 or CerS-mediated de novo biosynthesis), ceramide depletion was protective for mitochondria in astrocytes.

When evaluating time-lapse images of mitochondria labeled with MitoTracker or CytoPaint, we noticed that numerous mitochondria in nSMase2-deficient or FBI-treated

astrocytes were rapidly moving, while those in wild-type cells were predominantly resting (supplemental Movies, supplemental Fig. S2A–C). Increase of mitochondrial motility by ceramide depletion was unexpected and has not been described before. Motility was quantified by determining colocalization of individual mitochondria in consecutive time frames of time-lapse images and comparing wild-type with nSMase2-deficient astrocytes. Mitochondria at the cell periphery of nSMase2-deficient astrocytes showed about 30% higher motility than those in wild-type cells, while mitochondria close to the nucleus were almost immotile (Fig. 1E, F). These results indicated an unknown function of ceramide in the regulation of mitochondrial distribution or motility.

### Ceramide is enriched in mitochondrial-associated membranes and codistributes with microtubules and tubulin

To begin testing the role of ceramide in mitochondria, we visualized the distribution of ceramide within cellular compartments important for mitochondrial motility using a rabbit polyclonal anti-ceramide antibody originally developed in our laboratory (24). **Figure 2A, B** shows that the ceramide label codistributed with sigma 1 receptor (SigmaR1), a marker for MAMs, and MitoTracker, a marker for mitochondria. In nSMase2-deficient or FBI-treated wild-type cells, codistribution of ceramide label with MAMs and mitochondria was significantly reduced (Fig. 2B; supplemental Fig. S2D, E), indicating that ceramide generated by both nSMase2 and CerS is critical for ceramide enrichment in a subpopulation of MAMs, particularly in the cell periphery (arrows in Fig. 2B). We refer to this compartment as ceramide-enriched MAMs or CEMAMs.

Because peripheral mitochondria in ceramide-depleted cells showed higher motility, we tested to determine whether ceramide depletion would alter the distribution of CEMAMs along microtubules. **Figure 2C** shows that codistribution of the ceramide label with acetylated tubulin was significantly reduced in nSMase2-deficient astrocytes. The morphological appearance of ceramide-labeled vesicular and tubular structures along microtubules (arrows in Fig. 2C, left panel) in wild-type cells prompted us to analyze the codistribution of ceramide with microtubules at higher resolution. **Figure 3A, B** shows that ceramide was colabeled with microtubules and appeared to form contact structures that were also detected by super-resolution fluorescence microscopy (NSTORM, arrows in Fig. 3B, C). Codistribution of ceramide with acetylated tubulin was also detected in astrocytes in tissue sections of mouse brain, confirming the results obtained with cell cultures (supplemental Fig. S3A). The results obtained with anti-ceramide rabbit IgG were confirmed using anti-ceramide mouse IgM, another antibody reported to detect ceramide using immunocytochemistry (supplemental Fig. S3B) (24, 65). Despite partial overlap, the distribution of ceramide and acetylated tubulin was not identical, consistent with the assumption that ceramide is primarily enriched in CEMAMs associated with microtubules as well as mitochondria. **Figure 3D** shows that ceramide was codistributed with mitochondria and

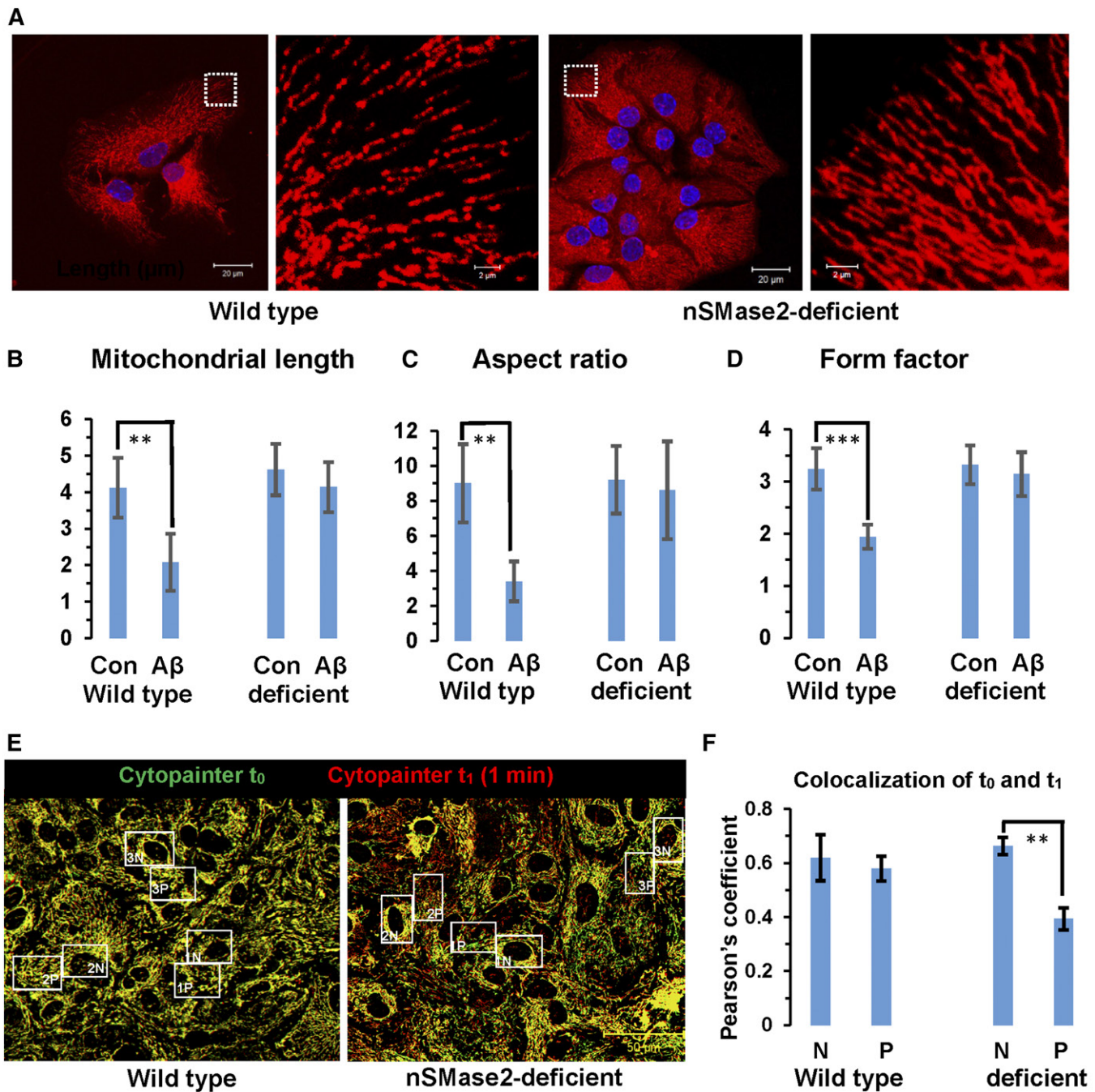


**Fig. 1.** Ceramide depletion increases resistance to A $\beta$  and mitochondrial motility. **A:** Wild-type and nSMase2-deficient astrocytes were incubated overnight with 1  $\mu$ M A $\beta_{1-42}$  and mitochondrial morphology recorded after labeling with MitoTracker (pseudocolored in red). Panels on right side show details of panels on left side. Scale bars = 20  $\mu$ m (left) and 2  $\mu$ m (right). **B–D:** Morphometric analysis of mitochondria from wild-type and nSMase2-deficient astrocytes with (A $\beta$ ) or without [control (Con)] A $\beta$  treatment. Mitochondrial length [ $**P < 0.01$  (B)], aspect ratio [ $**P < 0.01$  (C)], and form factor [ $***P < 0.001$  (D)] were calculated using ImageJ ( $n = 3$  independent cell cultures with five randomly selected areas per culture). **E, F:** Mitochondrial motility. Fifteen frames (one frame per minute) of wild-type and nSMase2-deficient astrocytes were recorded using time-lapse in vivo imaging. Mitochondria were labeled with CytoPainter ( $t_0$  pseudocolored in green,  $t_1$  pseudocolored in red). Motility of perinuclear (N) and peripheral (P) mitochondria was quantified using colocalization analysis (ImageJ) in two consecutive time frames ( $t_0$  and  $t_1$ ) ( $n = 3$  independent cell cultures with five randomly selected areas per culture;  $**P < 0.01$ ; scale bar = 50  $\mu$ m).

$\beta$ -tubulin, suggesting that potential interaction of ceramide with tubulin is important for the regulation of mitochondrial function and motility.

#### Tubulin is cross-linked to pacFACer and binds to ceramide

Our earlier studies showed that tubulin was coimmunoprecipitated when pulling down intracellular vesicles using

the anti-ceramide antibody (20). However, whether tubulin interacts directly with ceramide and what the function of this potential interaction is remained unclear. To test this, we used a bifunctional ceramide analog (pacFACer) that can be UV-cross-linked to ceramide binding proteins and then derivatized by click chemistry with fluorophores or biotin, a novel labeling technique recently developed

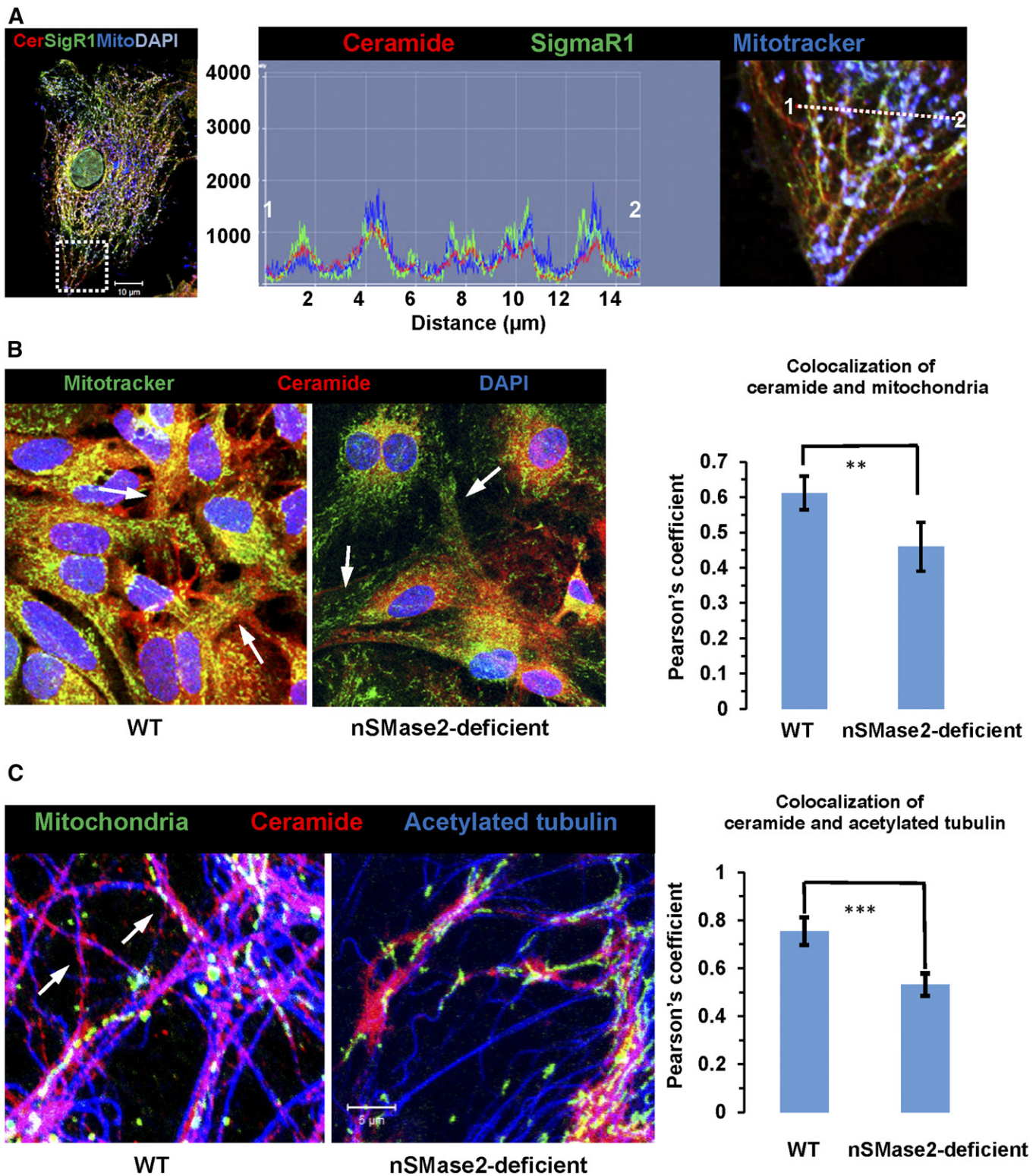


**Fig. 2.** Ceramide is colocalized with MAMs, peripheral mitochondria, and microtubules, which is prevented by nSMase2 deficiency and FB1 treatment. **A:** Immunocytochemistry using MitoTracker (pseudocolored in blue) and antibodies against ceramide (rabbit IgG, pseudocolored in red) and SigmaR1 (goat IgG, pseudocolored in green). The left panel shows the overview with the inset frame at higher resolution shown in the right panel. The middle panel shows the profile of fluorescence signal intensity along the dashed line in the right panel, indicating colabeling of ceramide and SigmaR1 at mitochondria (white color in image). The y-axis in the middle panel shows arbitrary units of fluorescence signal intensity. **B:** Colocalization of ceramide (pseudocolored in red) with MitoTracker (pseudocolored in green) in WT and nSMase2-deficient astrocytes. The arrows point at peripheral mitochondria ( $n = 5$  independent cultures;  $**P < 0.01$ ). **C:** Colocalization of ceramide (pseudocolored in red) and acetylated tubulin (pseudocolored in blue) in WT and nSMase2-deficient astrocytes. Mitochondria are pseudocolored in green ( $n = 4$  independent cultures;  $***P < 0.001$ ).

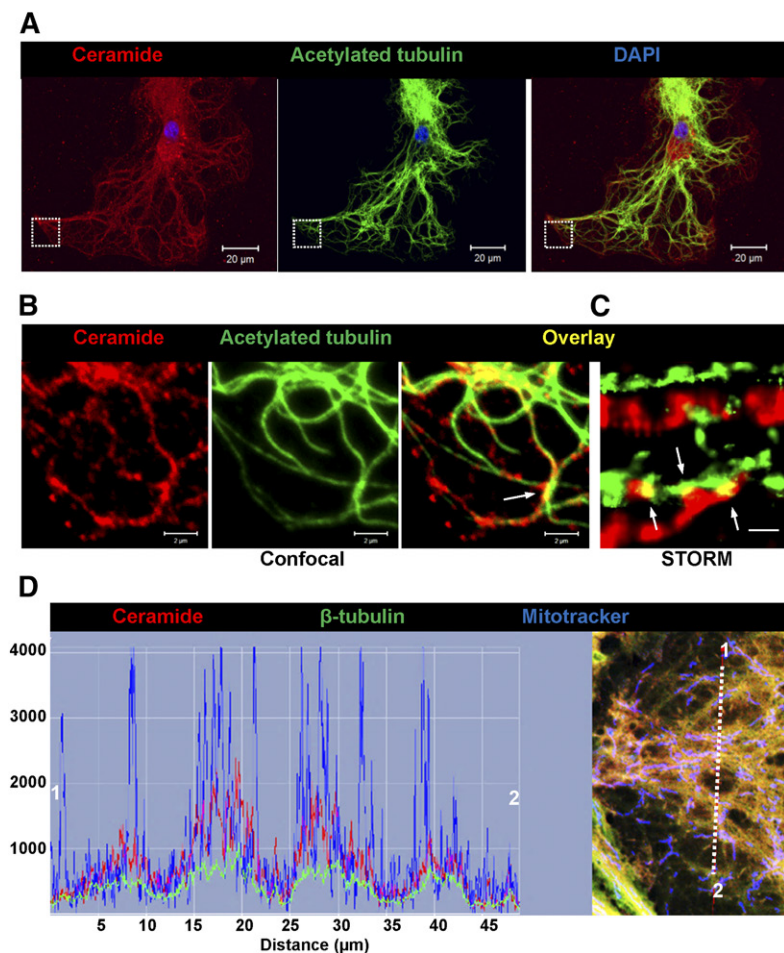


**Fig. 3.** Ceramide forms contact structures with microtubules and codistributes with tubulin. **A:** Confocal immunofluorescence microscopy using anti-ceramide rabbit IgG (pseudocolored in red) and anti-acetylated tubulin mouse IgG (pseudocolored in green). The image shows Z-scan projection onto one plane. Scale bar = 20  $\mu\text{m}$ . **B:** The image shows detail from A (frame) at higher magnification. Scale bar = 2  $\mu\text{m}$ . **C:** NSTORM using antibodies as described in A. Arrows point at potential contact structures (yellow) between ceramide (CEMAM) and microtubules. Scale bar = 500 nm. **D:** Confocal immunofluorescence microscopy using astrocytes labeled with MitoTracker (pseudocolored in blue) and then subjected to immunocytochemistry with anti- $\beta$ -tubulin mouse IgG (pseudocolored in red) and anti-ceramide rabbit IgG (pseudocolored in green). The right panel shows fluorescence signal intensity and distribution indicating colocalization of antigens at mitochondria.

for sphingolipids (19, 66–68). In addition, we used ceramide-linked agarose beads to pull down and identify ceramide binding proteins from cell lysates.

In a cell-free assay, lipid-adsorptive ELISA plates were coated with pacFACer and then incubated with purified tubulin from pig brain. After UV cross-linking, unbound tubulin was washed out and the cross-linked protein tagged with Cy7.5 and then eluted with SDS sample buffer. **Figure 4A, B** shows that only tubulin exposed to UV was labeled (lanes 7 and 9, arrow), while the control (without UV) remained unlabeled (lanes 6 and 8). BSA was not significantly cross-linked to pacFACer (Fig. 4A, B, lanes 4 and 9), although its concentration was more than 10-fold of that of tubulin (1 mg/ml vs. 0.08 mg/ml). A proteomics analysis of Cy7.5-labeled tubulin (Fig. 4A, B, lanes 7 and 9) led to the identification of the tryptic peptide,  $M_{363}$ AATFIGN-STAIQELFK<sub>379</sub>, in the  $\beta$ -tubulin isoform tubb4a (UniProt accession number F2Z5K5) as the candidate sequence cross-linked to pacFACer.

A preliminary modeling analysis of potential ceramide binding sites using the UCSF Zinc database (C16:0 ceramide, zinc\_40164304.mol2), RCSB PDB database ( $\alpha\beta$  tubulin dimer, ijff.pdb), and Swissdocks program suggested three potential ceramide binding sites in the dimer (supplemental Fig. S3C) with binding energies of more than 8 kcal/mol (equivalent to an equilibrium constant of  $<1 \mu\text{M}$ ). As a comparison, the intracellular tubulin

concentration can go up to about 1 mg/ml or 20  $\mu\text{M}$ , which is slightly above the threshold for microtubule self-assembly (0.8 mg/ml) (69, 70). Site 1 was close to the maytansine and GTP binding sites in the vicinity of helices H3-H3' (71). Site 2 was similar to the taxol binding site close to the M-loop region (72). Site 3 was in proximity to the C-terminal helices H10-H11 and overlapped with the peptide identified by proteomics analysis (supplemental Fig. S3C, D). The molecular modeling analysis was consistent with the results from pacFACer cross-linking and may therefore represent potential binding sites for ceramide in  $\alpha$ - and  $\beta$ -tubulin.

To confirm cross-linking to cellular tubulin, homogenized astrocytes were incubated with pacFACer and the cross-linked protein tagged with biotin followed by streptavidin pull-down. Proteomics analysis and immunoblotting suggested that  $\beta$ -tubulin (UniProt accession number P99024) was pulled down from the cross-linked sample (Fig. 4C, lane 3). Tubulin was not significantly cross-linked to other photoactivatable lipids, including photoactivatable fatty acid and sphingosine, demonstrating specificity of the reaction with pacFACer (67, 68, 73). In addition, we used ceramide-linked agarose beads to test which tubulin isoforms from a cellular homogenate bind to ceramide (Fig. 4D, lane 2). Proteomics analysis of the eluate showed that various  $\alpha$ -tubulin (P68369, P05213, P68373, and Q9JJZ2) and  $\beta$ -tubulin (P99024, P68372, Q7TMM9, Q9ERD7, and



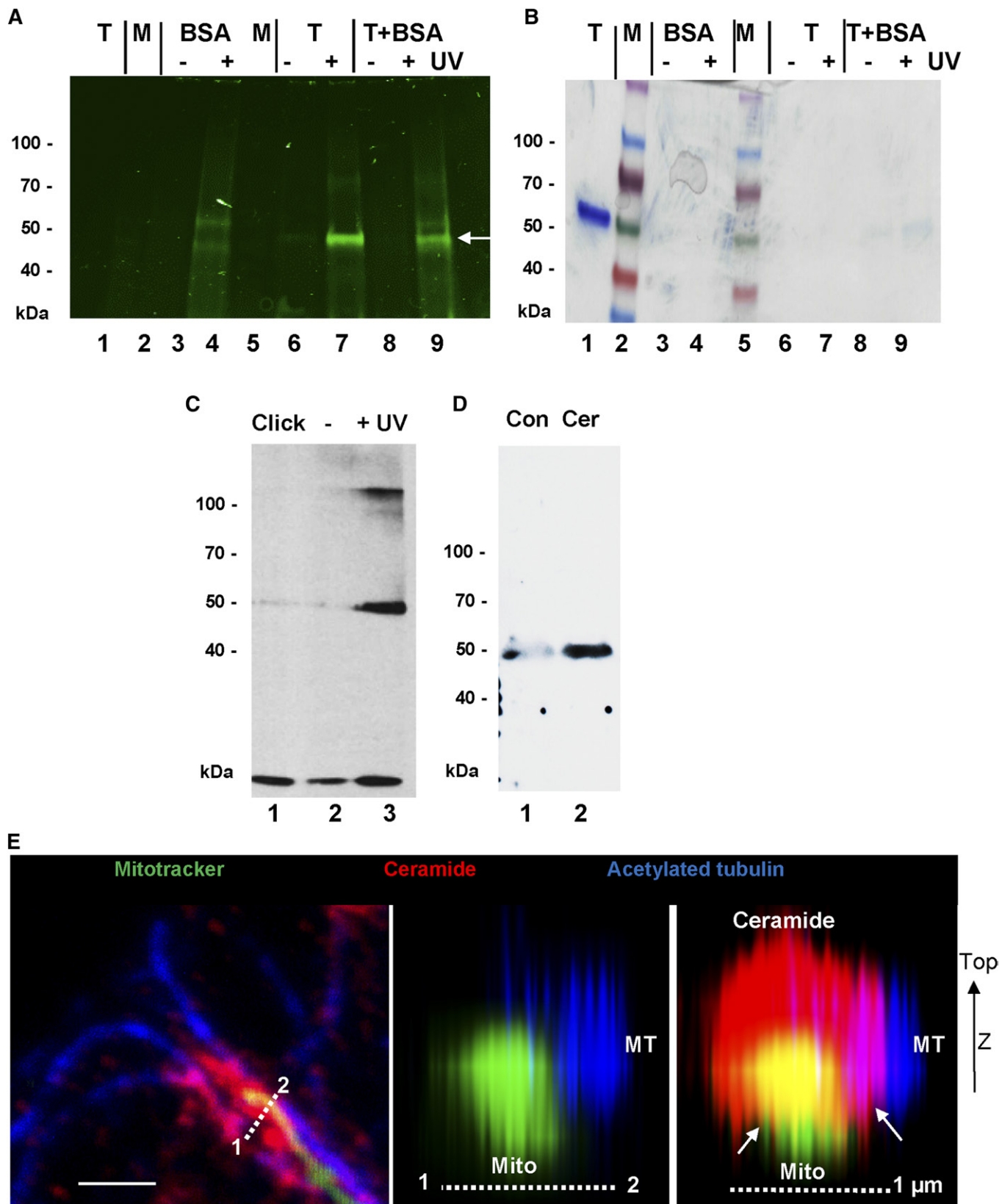


**Fig. 4.** Cross-linking of pacFACer to tubulin and binding to ceramide. A, B: Tubulin from pig brain was cross-linked to pacFACer, tagged with Cy7.5 azide, and then separated by SDS-gel electrophoresis [fluorescence scanning (A); Coomassie staining (B)]. Lane 1, control tubulin (1  $\mu$ g); lane 2, protein standard; lane 3, BSA - UV; lane 4, BSA + UV; lane 5, protein standard; 6, tubulin - UV; lane 7, tubulin + UV; lane 8, tubulin + BSA - UV; lane 9, tubulin + BSA + UV. The arrow points at the tubulin band. C: Protein from astrocytes was cross-linked to pacFACer, tagged with biotin azide, and the protein pulled down with streptavidin agarose beads. Immunoblot was performed using  $\beta$ -tubulin mouse IgG Lane 1, click reaction without pacFACer; lane 2, with pacFACer - UV; lane 3, with pacFACer + UV. D: Pull-down of protein with control agarose (Con) or ceramide-linked agarose beads (Cer). The immunoblot of protein in the eluate was probed with

Q922F4) isoforms were among the ceramide-binding proteins. Immunocytochemistry at higher resolution showed that ceramide colabeled with contact structures between microtubules and mitochondria (Fig. 4E, arrows), suggesting that ceramide is important for the function of membranous contact sites between microtubules and mitochondria.

#### **pacFACer-cross-linked tubulin is translocated from the perinuclear region to peripheral CEMAMs and codistributes with ceramide**

Based on the observation that pacFACer was cross-linked to tubulin, we investigated to determine whether intracellular pacFACer label colocalized with ceramide and tubulin at CEMAMs, mitochondria, or microtubules. Initially, we immediately fixed astrocytes after pacFACer incubation and UV cross-linking (0 h post-cross-linking), a procedure described for other bifunctional sphingolipid analogs with only minimal metabolic turnover of ceramide into other sphingolipid derivatives that may cross-link to proteins (68). In contrast to these previous studies, we also introduced a post-cross-linking incubation step (24 h), allowing intracellular trafficking of the pacFACer-linked protein. pacFACer remaining in the cell, but not cross-linked and further metabolized to other sphingolipid analogs (e.g., sphingomyelin), was washed out with methanol following fixation. The pacFACer-linked protein was visualized using click chemistry-mediated tagging with fluorophores.

Fixation immediately after cross-linking (0 h post-cross-linking) led to pacFACer labeling of a perinuclear compartment (Fig. 5A) that partially colocalized with calnexin, a chaperone and calcium regulator found in the ER and some ER-derived subcompartments, such as MAMs (Fig. 5C) (74). There was little or no distribution of pacFACer to the cell periphery (area labeled P in Fig. 5C). The pacFACer-labeled compartment also partially colocalized with GM130 (supplemental Fig. S3E), a golgin family protein important for microtubule assembly and ER-to-Golgi trafficking (75), suggesting that initial cross-linking of pacFACer to protein was limited to the perinuclear ER and/or Golgi. Incubation for 24 h post-cross-linking led to the gradual appearance of pacFACer labeling in the cell periphery (Fig. 5B, D). Figure 5E shows imaging results obtained after ectopic expression of the GFP-tagged ER marker protein, Sec61 (Sec61-GFP), in HEK293T cells. Codistribution of the pacFACer label with Sec61-GFP (solid arrows) and MitoTracker (dashed arrows) was consistent with the results obtained with pacFACer cross-linking in astrocytes.

Next, we tested to determine whether pacFACer and ceramide were codistributed in the same compartment(s), particularly microtubules, MAMs, and mitochondria. **Figure 6A–C** shows that pacFACer and ceramide were colabeled with isoforms of tubulin along microtubules. Colabeling was also detected in MAMs (arrows in Fig. 6D), suggesting

that pacFACer-cross-linked protein was transported to CEMAMs to contact structures with microtubules and mitochondria. **Figure 7A–E** shows that pacFACer and ceramide were codistributed at peripheral mitochondria (arrows in Fig. 7A) along microtubules (arrows in Fig. 7B). Using higher resolution confocal microscopy (Fig. 7C) and STORM (Fig. 7D), we found that codistribution of pacFACer with ceramide was limited to contact structures (arrows in Fig. 7D, right panel), consistent with the assumption that pacFACer-cross-linked tubulin was localized in CECs, particularly CEMAMs that formed attachment sites with microtubules and mitochondria, as shown in Fig. 4E (arrows).

Similar to the effect of ceramide depletion on the distribution of CEMAMs (Fig. 2B), we tested to determine whether nSMase2 deficiency reduced colabeling of pacFACer with mitochondria. While nSMase2 deficiency did not significantly change codistribution of pacFACer with mitochondria located closer to the nucleus (area of interest labeled N), there was a significant reduction of label at peripheral mitochondria (area of interest labeled P) in nSMase2-deficient astrocytes (Fig. 7E, F). Taken together, these results suggested that after initial cross-linking in the perinuclear ER (or Golgi), pacFACer-cross-linked tubulin was distributed to CEMAMs and mitochondria, which was prevented by ceramide depletion.

#### **Ceramide depletion reduces association of ceramide with tubulin at mitochondria**

Our results were consistent with the assumption that tubulin was cross-linked to pacFACer and transported to CEMAMs. Therefore, we tested to determine whether ceramide was associated with tubulin at CEMAMs, and whether CAT formation or distribution was reduced by ceramide depletion in nSMase2-deficient or FB1-treated astrocytes. Apart from cross-linking of pacFACer, there is currently no assay able to visualize direct binding of ceramide to a particular protein in intact cells. Recently, PLAs have been developed to detect formation of protein or other complexes by immunocytochemistry. PLAs use short cDNA strands attached to secondary antibodies to amplify a fluorescence signal by rolling circle PCR if the primary antibodies are in close vicinity (<40 nm), indicating complex formation of the antigens (76, 77). To date, the anti-ceramide IgG is the only ceramide-specific antibody that can be used for PLA with commercially available secondary antibodies.

**Figure 8A–D** shows that PLA signals using anti-ceramide [rabbit IgG (+) strand secondary antibody] and anti- $\beta$ -tubulin [mouse IgG (–) strand secondary antibody] were predominantly associated with cross-linked pacFACer and MitoTracker labeling, suggesting that CAT complexes are formed at contact structures of CEMAMs with mitochondria. Pairing nonspecific rabbit IgG or mouse IgG with anti-rabbit IgG (+) and anti-mouse IgG (–) did not yield

---

anti-detyrosinated  $\alpha$ -tubulin rabbit IgG. E: High-resolution confocal microscopy showing arrangement of microtubules (MT), mitochondria (Mito), and ceramide (middle and right panels show z-stack reconstruction along dashed line in the left panel). The arrows point at contact structures of ceramide (CEMAM) with microtubules and mitochondria.

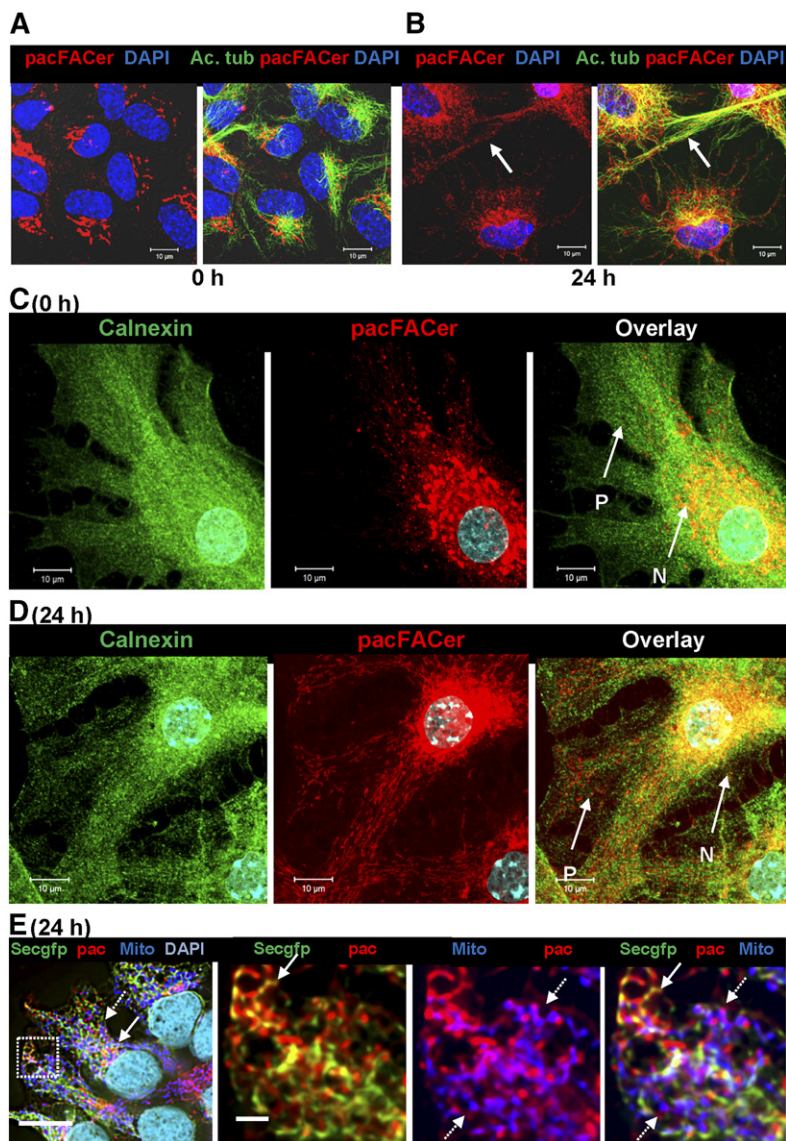


**Fig. 5.** Protein cross-linked to pacFACer is transported from the perinuclear region to the cell periphery. A, B: Primary cultured astrocytes were incubated with pacFACer and either immediately fixed after cross-linking (A) or incubated for another 24 h prior to fixation (B) and subjected to click chemistry-mediated labeling with Alexa647-azide (pseudocolored in red) and immunocytochemistry using an antibody against acetylated tubulin (mouse IgGs, pseudocolored in green). C, D: Experiment performed as in A and B, and immunolabeled for calnexin (mouse IgG, pseudocolored in green). N, perinuclear region; P, cell periphery. Scale bars = 10  $\mu$ m. E: HEK293T cells expressing the ER marker, Sec61-GFP (Secgfp) (pseudocolored in green), cross-linked with pacFACer (pac) (pseudocolored in red, solid arrows), and labeled with MitoTracker (Mito) (pseudocolored in blue, dashed arrows). The left panel is an overview with framed area shown at high resolution in the middle and right panels. Scale bars = 20 (left panel) and 2  $\mu$ m (middle and right panels).

PLA signals demonstrating specificity of the method (not shown). It should be noted that at higher resolution, the dot-like PLA signal did not exactly codistribute with the antigens or site of antibody binding, but rather showed a stalk-drop appearance (arrows in Fig. 8D) as the signal for ceramide-tubulin interaction colocalized with pacFACer-labeled mitochondria (dashed arrows point at the initial binding sites for the secondary antibodies). The number of PLA signals was reduced in nSMase2-deficient astrocytes and cells (astrocytes and HEK293T) treated with the CerS inhibitor, FB1 (Fig. 8B, E, left panel, only HEK293T cells are shown), consistent with decreased colocalization of ceramide and pacFACer at mitochondria. Figure 8F confirms colocalization of the PLA signal for the CAT complex with mitochondria (arrows).

#### Ceramide depletion reduces complex formation between tubulin and VDAC1 and increases cellular ATP levels

The formation of CAT complexes and its reduction by ceramide depletion implies that association with ceramide may regulate the function of tubulin at mitochondria.

Previous studies showing that tubulin closes VDAC1 suggested that CAT may regulate VDAC1 (52, 54, 78). We performed PLAs for CAT-dependent formation of VDAC1-tubulin complexes using anti-VDAC1 [rabbit IgG (+)] and anti- $\alpha$ - or - $\beta$ -tubulin [mouse IgG (-)] antibodies with wild-type and nSMase2-deficient astrocytes. **Figure 9A, B** and supplemental Fig. S4A, B show that nSMase2 deficiency or FB1-mediated inhibition of CerSs led to 70% reduction of the number of PLA signals for complex formation between VDAC1 and tubulin. Image analysis at higher resolution confirmed that the signals indicating VDAC1-tubulin complexes were located at mitochondria (Fig. 9C, D, supplemental Fig. S4C), consistent with the localization of CATs (Fig. 8D, F).

To confirm the validity of the PLA results, we performed coimmunoprecipitation assays using anti- $\alpha$ -tubulin mouse IgG for the immunoprecipitation and anti-VDAC1 rabbit IgG for the immunoblotting reaction with HEK293T cells with or without FB1 treatment. Figure 9E, F shows that in HEK293T cells, the number of PLA signals for the VDAC1-tubulin complex was reduced by ceramide depletion to the

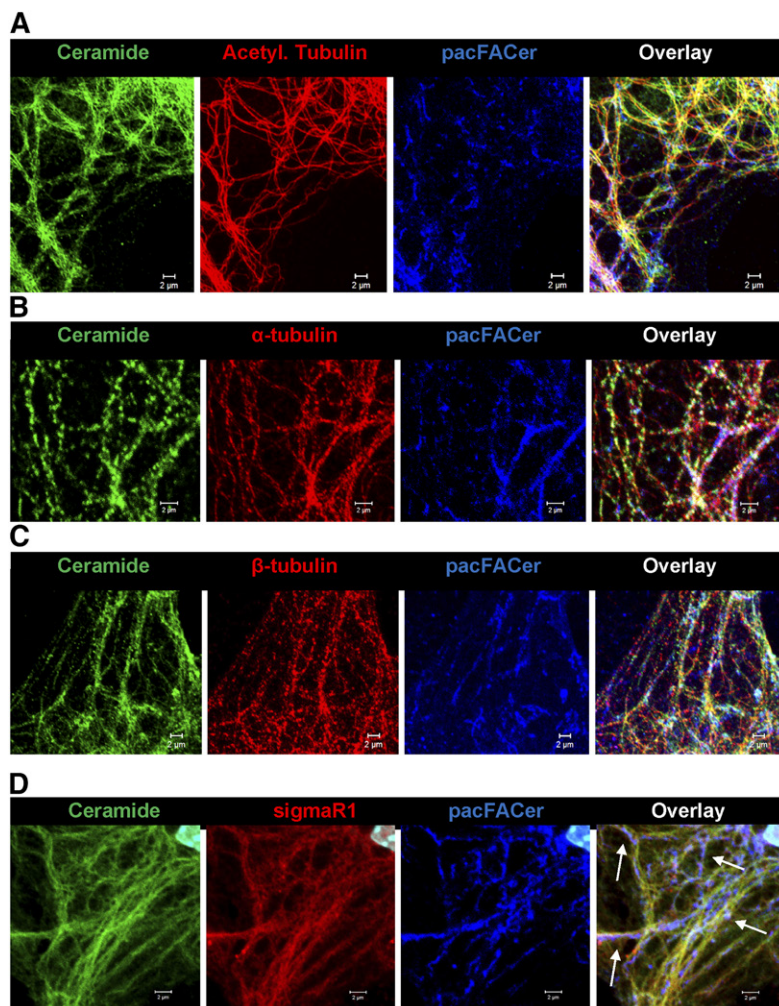


**Fig. 6.** Protein cross-linked to pacFACer colocalizes with ceramide at microtubules and CEMAMs in the cell periphery. A–C: Confocal immunofluorescence microscopy (Z-scan projections) using primary astrocytes subjected to pacFACer cross-linking and tagging with Alexa647 azide (24 h post-cross-linking, pseudocolored in blue) and antibodies against ceramide (rabbit IgG, pseudocolored in green) and acetylated tubulin [mouse IgG (A)],  $\alpha$ -tubulin [mouse IgG (B)],  $\beta$ -tubulin [mouse IgG (C)], or  $\beta$ -tubulin tubb4/5 [mouse IgG (D)] all pseudocolored in red. Scale bars = 2  $\mu$ m. D: Same as in A–C, but using antibody against SigmaR1 (goat IgG, pseudocolored in red). The arrows point at pacFACer-labeled CEMAMs.

same extent as with astrocytes (supplemental Fig. S4A, B). For the coimmunoprecipitation experiment, digitonin (1%) was used as a detergent because it is known to preserve the membrane environment in ceramide biosynthesis and it is commonly used for solubilization of proteins from the OMM (79–81). Figure 9G shows that ceramide depletion reduced the amount of coimmunoprecipitated VDAC1 (nontreated cells and nonspecific mouse IgG were used as controls) consistent with the decrease of the number of PLA signals for the VDAC1-tubulin complex in HEK293 cells (Fig. 9E, F). The reverse immunoprecipitation reaction using anti-VDAC1 rabbit IgG and anti- $\alpha$ -tubulin for immunoblotting did not show a signal, possibly due to inaccessibility of VDAC1 to its antibody in digitonin-solubilized membranes (not shown).

While tubulin-mediated closure of the VDAC1 channel was shown to block ADP/ATP transport, the effect of this regulation on the intracellular ATP concentration has not been reported yet. There are numerous reports, however, that VDAC1 downregulation profoundly decreases levels of intra- and extracellular (secreted) ATP (45, 46, 82). Based on our observation that ceramide depletion decreases complex formation between tubulin and VDAC1, we tested to determine whether reducing ceramide would upregulate cellular ATP levels. Figure 9H, I shows that ATP levels

of nSMase2-deficient or FBI-treated astrocytes were 40% higher than those in wild-type controls. Increase of cellular ATP by ceramide depletion was consistent with higher mitochondrial motility and resistance to A $\beta$ , although further research is needed to understand these potentially related effects. Notwithstanding this limitation, our research strongly suggests that there is a novel function of ceramide for mitochondria regulating ATP levels, motility, and resistance to A $\beta$  mitotoxicity.

## DISCUSSION

For two decades, research on ceramide in mitochondria was focused on its role in the induction of apoptosis. This focus appeared justified because strong experimental evidence supported the notion that ceramide generated by SMase(s) at mitochondria induced apoptosis, probably by forming channels for pro-apoptotic proteins in the OMM (59, 61, 83–85). However, the abundance of ceramide in MAMs under physiological conditions also suggested other functions of ceramide that were only poorly understood. Compartmentalization of ceramide in microdomains (rafts) or more extended membrane areas and its physiological function remained elusive. About 10 years ago, our laboratory developed a polyclonal ceramide antibody that proved

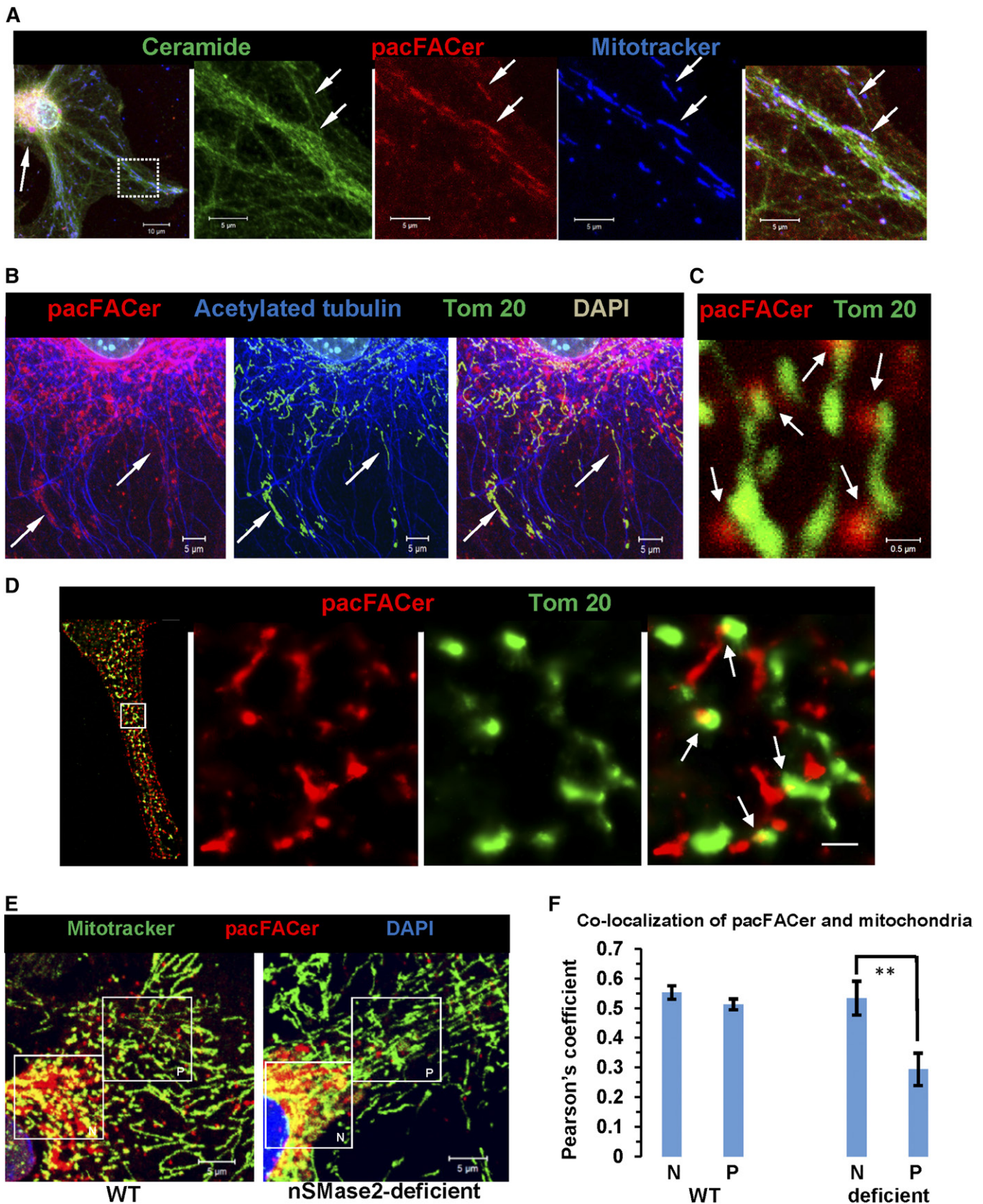


**Fig. 7.** Protein cross-linked to pacFACer colocalizes with ceramide at mitochondria in cell periphery, which is prevented in nSMase2-deficient cells. **A:** Astrocytes subjected to pacFACer cross-linking and labeled with MitoTracker (24 h post-cross-linking, pseudocolored in blue) underwent click chemistry-mediated tagging with Alexa647 azide (pseudocolored in red) and immunocytochemistry using anti-ceramide rabbit IgG (pseudocolored in green). The left panel shows an overview with panels on the right showing details of the framed area at high resolution. The arrow in the left panel points at the perinuclear region with codistribution of pacFACer and ceramide. The arrows in the panels on the right point at peripheral mitochondria colabeled for ceramide and pacFACer. **B:** pacFACer/Alexa647-tagged protein

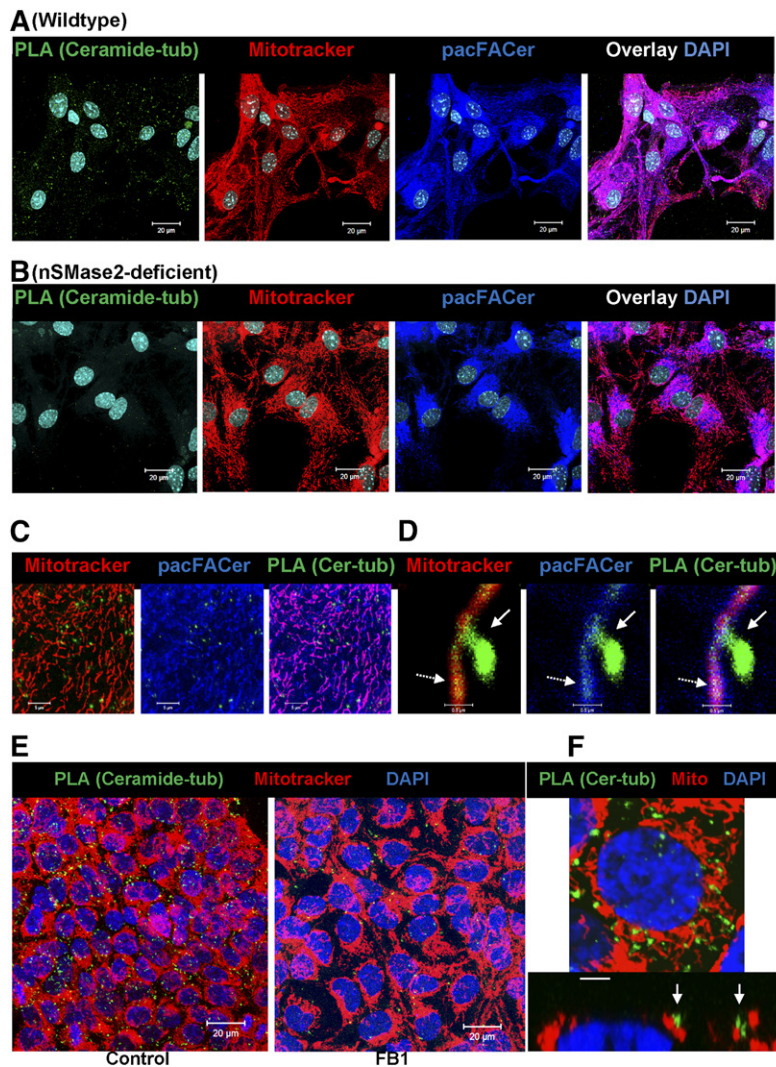


**Fig. 8.** Ceramide depletion reduces formation of CAT complexes at mitochondria. A–D: PLAs indicating complex formation between ceramide and tubulin in astrocytes. Astrocytes subjected to pacFACer cross-linking and labeled with MitoTracker (24 h post-cross-linking, pseudocolored in red) underwent click chemistry-mediated tagging with Alexa647 azide (pseudocolored in blue) and PLAs using anti-ceramide rabbit IgG (+) and anti  $\beta$ -tubulin mouse IgG (–) (PLA pseudocolored in green) in WT and nSMase2-deficient astrocytes. Images are shown at higher magnification and association of PLA signals with pacFACer-labeled mitochondria (C, D). Stalk-drop appearance (solid arrow) of high resolution PLA signal attached to mitochondrion (dashed arrow, initial attachment site of secondary antibodies) (D). E, F: PLA using HEK293T cells, anti-ceramide rabbit IgG (+), and anti- $\alpha$ -tubulin mouse IgG (–). Signals for CAT complexes are pseudocolored in green; MitoTracker is pseudocolored in red. Scale bars = 20  $\mu$ m. F: Detail with arrows pointing at PLA signal at mitochondria (Z-scan in bottom panel). Scale bar = 2  $\mu$ m.

useful for visualizing ceramide in fixed cells and tissues using immunocytochemistry (24). It was shared with many other laboratories to determine the intracellular distribution of ceramide and was instrumental to our research on CECs (18–21, 25, 27). Most recently, this antibody allowed the visualization of ceramide rafts using super-resolution microscopy (dSTORM) (18), clearly demonstrating that the distribution of ceramide in cellular membranes is anisotropic and regulated by SMase(s).

In addition to anti-ceramide IgG, a new generation of ceramide analogs was developed to use click chemistry-mediated addition of fluorophores after the analog inserted into cellular membranes (66, 86). We and our collaborators showed that these analogs are codistributed with CECs

detected by the antibody (25). Using a modified version of these analogs, bifunctional ceramide analogs (pacFACer) that can be UV-cross-linked to ceramide binding proteins and derivatized using click chemistry, we demonstrated that pacFACer can be cross-linked to protein in CECs (19). In the present study, we discovered that CEMAMs contain protein cross-linked to pacFACer. While it is currently not possible to clearly identify the cross-linked protein by immunocytochemistry, pull-down assays and PLAs suggest that tubulin is a protein bound by ceramide in CEMAMs. This assumption is supported by the observation that ceramide depletion by nSMase2 deficiency or CerS inhibition with FB1 reduces the number of PLA signals at mitochondria when using anti-ceramide and tubulin antibodies.

(pseudocolored in red) is colocalized with peripheral mitochondria (Tom 20, pseudocolored in green) along microtubules (acetylated tubulin, pseudocolored in blue). C, D: Confocal immunofluorescence microscopy [Z-scan projection onto one plane (C)] and NSTORM super resolution fluorescence microscopy of pacFACer-cross-linked protein tagged with Alexa647 azide [pseudocolored in green (D)] combined with anti-Tom 20 rabbit IgG (Atto488, pseudocolored in green). The panel on the left side in D shows an overview of the NSTORM image; the panels on the right show details of the frame in the left panel. The arrows indicate colocalization at potential contact sites between ceramide (CEMAMs) and mitochondria. Scale bar = 500 nm. E, F: Colocalization of pacFACer (pseudocolored in red) and MitoTracker (pseudocolored in green) in WT and nSMase2-deficient astrocytes. The frames in the figure panels indicate perinuclear (N) and peripheral (P) mitochondria, respectively (scale bar = 5  $\mu$ m; n = 5 independent cell cultures with five randomly selected areas per culture; \*\* $P < 0.01$ ).

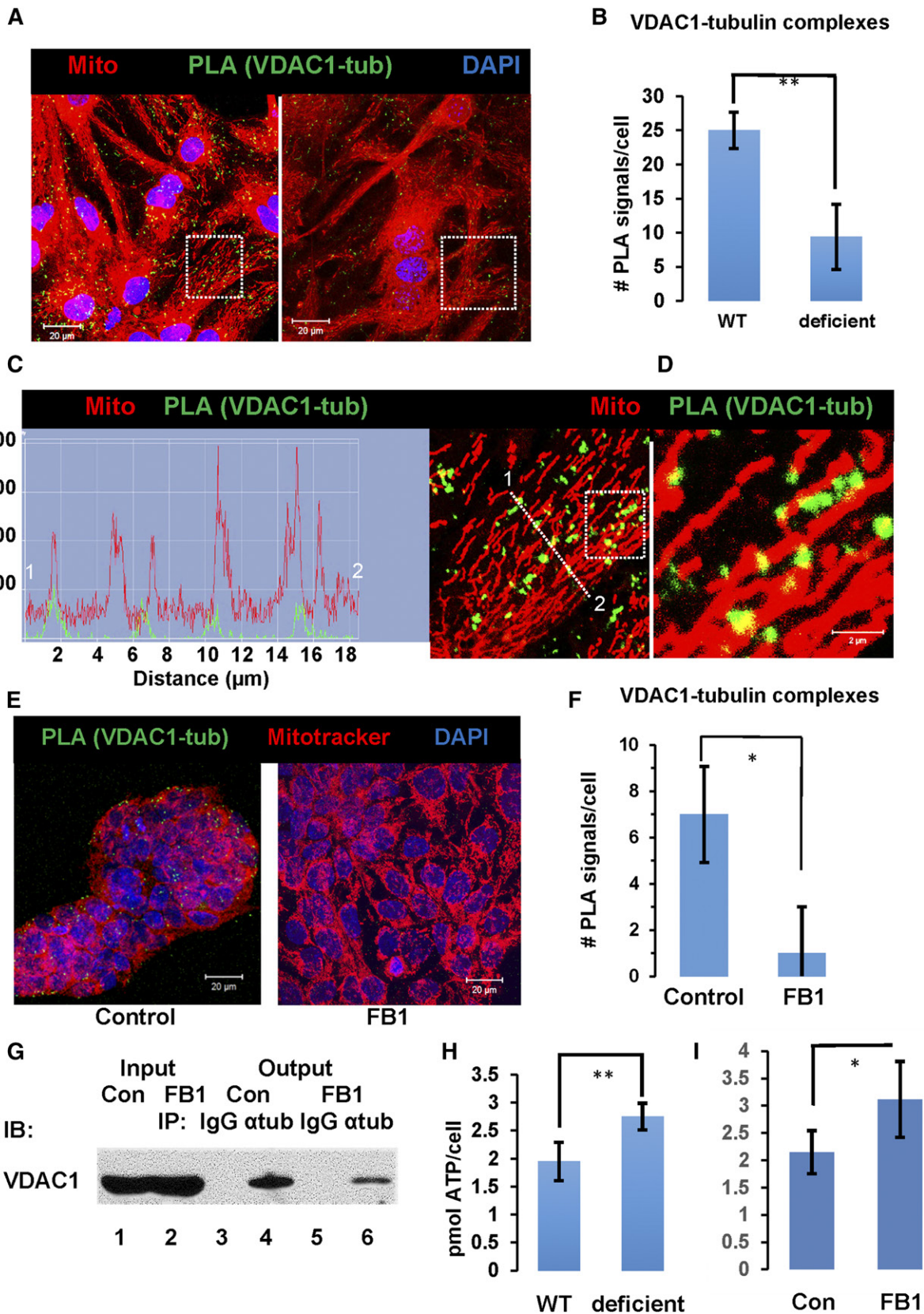


**Fig. 9.** Ceramide depletion reduces VDAC1-tubulin complex formation at mitochondria and increases intracellular ATP levels. A–D: Astrocytes were labeled with MitoTracker (pseudocolored in red) and PLAs performed using anti-VDAC1 rabbit IgG (+) and anti- $\beta$ -tubulin mouse IgG (–) (PLA pseudocolored in green). B: Quantitation of VDAC1-tubulin complexes in WT and nSMase2-deficient astrocytes ( $n = 4$  independent cell cultures;  $**P < 0.01$ ). C: Detail from A (frame in left panel) and fluorescence signal intensity profile indicating association of PLA signals with mitochondria. D: Detail from C (frame). E, F: PLA using anti-VDAC1 rabbit IgG (+) and anti- $\alpha$ -tubulin mouse IgG (–) with nontreated and FB1-treated HEK293T cells. Signals for VDAC1-tubulin complexes are pseudocolored in green, MitoTracker is

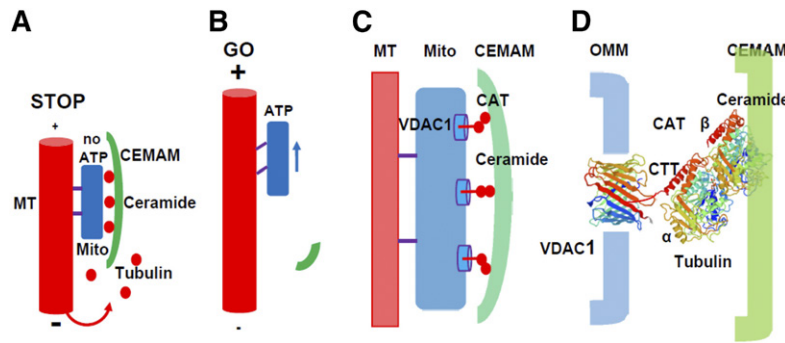


**Fig. 10.** Hypothetical mechanism of VDAC1 closure by CAT in CEMAMs. A: Elevated cytosolic tubulin levels due to increased microtubule disassembly/reduced assembly lead to association of tubulin with ceramide in CEMAM-resident CATs that wrap around mitochondria and block VDAC1-mediated ADP/ATP transport between mitochondria and the cytosol. Lack of ATP leads to inactivation of motor proteins and mitochondria stop moving (STOP mode). B: When microtubules extend to the periphery, cytosolic (free) tubulin concentration is low, VDAC1 unblocked, and ATP available to drive mitochondria transport along microtubules (GO mode). Higher ceramide levels facilitate ATP deprivation and the STOP mode, while low ceramide levels favor ATP release and the GO mode. This leads to higher mitochondrial motility in nSMase2-deficient or FB1-treated astrocytes. C, D: Potential arrangement and ceramide binding of  $\alpha\beta$  tubulin dimers interacting with VDAC1 in the OMM. Note that binding of  $\beta$ -tubulin to ceramide in CATs is likely to be mediated by protein domains defined as cluster 2 from molecular modeling shown in supplemental Fig. S3C, D. Also note that complex formation with VDAC1 is likely to be mediated by the dimer with  $\alpha$ -tubulin reaching into the VDAC1 pore with its C-terminal tail (CTT).

It should be noted, however, that any PLA signal is evidence for, but not absolute proof of, a complex because its components can still be about 40 nm apart.

Despite this caveat, there is solid evidence from independent studies that ceramide binds directly to tubulin (20, 28, 29). Molecular modeling predicts that the affinity of tubulin for ceramide is relatively low (0.5–1  $\mu$ M), which may turn CAT into a sensor for free tubulin at physiological levels in the cytosol to block VDAC1 and ATP release, provided that sufficient ceramide for CAT formation is available (Fig. 10A). On the other hand, if ceramide levels are low, formation of CAT is also reduced and ATP release and mitochondrial motility increased (Fig. 10B). Our model predicts that CEMAMs engage CAT into blocking VDAC1 in a zipper or Velcro-like way (Fig. 10C): simultaneous CAT formation in several complexes with VDAC1 will stabilize the contact of CEMAMs to the OMM despite presumably lower affinity for the individual ceramide-tubulin interaction. This interaction is likely to be mediated by a tubulin dimer with  $\beta$ -tubulin binding to ceramide and the C-terminal tail of (detyrosinated)  $\alpha$ -tubulin reaching into the VDAC1 channel (Fig. 10D).

Previous studies using a similar or the same ATP assay as applied in our study showed that VDAC1 downregulation leads to reduced levels of intracellular ATP (45, 46, 82). This observation is quite remarkable because this assay does not


distinguish between mitochondrial or cytosolic ATP levels, indicating that blocking VDAC1 will reduce both ATP pools. It should be noted, however, that the results of the ATP assay do not exclude the effect of ceramide on other ATP regulatory mechanisms, such as aerobic glycolysis or the activity of the adenine (ADP/ATP) nucleotide translocator (ANT), an ADP/ATP exchanger located in the inner mitochondrial membrane (87). The interaction of ANT with CerS6 has been reported to be involved in ceramide-induced prevention of permeability transition pore opening and calcium accumulation in mitochondria of oligodendrocytes (62). It remains to be determined whether the interaction of ceramide-enriched membrane domains with transporters and channels in the inner mitochondrial membrane, OMM, or MAM is part of a regulatory cascade or module to affect energy and calcium homeostasis in mitochondria.

There is some discrepancy in which VDAC isoform is more critical for regulation of intracellular ATP, which is likely to be cell-type specific (51, 52). Most recently, excess elevation of ceramide has been shown to induce mitophagy, suggesting that the physiological function of ceramide, as discussed in our study, requires limitation of its concentration at mitochondria (88, 89). While ATP levels observed in our study are consistent with CAT-regulated ATP release under normal physiological conditions, several studies have shown that, under pathophysiological conditions, reduction

pseudocolored in red (scale bars = 20  $\mu$ m; n = 4; \* $P$  < 0.05). G: Coimmunoprecipitation analysis of the VDAC1-tubulin complex in control (Con) and ceramide-depleted (FB1-treated) HEK293T cells. Input is protein after solubilization of mitochondria with 1% digitonin used for incubation with anti- $\alpha$ -tubulin mouse IgG or nonspecific mouse IgG (control). Output is protein eluted after pull-down with anti-mouse IgG gel beads and immunoblotted using anti-VDAC1 rabbit IgG. Ceramide depletion was achieved by incubation of cells for 60 h with 3  $\mu$ M FB1. Lane 1, input control cells; lane 2, input FB1-treated cells; lane 3, output control IgG with nontreated cells; lane 4, output anti- $\alpha$ -tubulin IgG with nontreated cells; lane 5, output control IgG with FB1-treated cells; lane 6, output anti- $\alpha$ -tubulin IgG with FB1-treated cells. H, I: ATP levels in WT (H) or control (Con) (I) and nSMase2-deficient (H) or FB1-treated (I) astrocytes (n = 4 independent cell cultures; \* $P$  < 0.05; \*\* $P$  < 0.01).



of ATP levels are concurrent with decreased mitochondrial motility and increased fragmentation (44, 90–92). The contribution of excess ceramide to this mitotoxicity is likely to include additional mechanisms, which will be explored in future studies. Likewise, there is discrepancy in the literature with respect to the effect of FBI on mitochondria. FBI has been shown to protect cells from apoptosis by reducing the effect of ceramide on mitochondria, but it has also been described to inhibit mitochondrial complex I and induce cell death (93–95). This discrepancy may be due to different FBI concentrations and incubation times, as well as the limitation that, in many of the previous studies, the effect of FBI was not compared with any other effects of ceramide depletion by enzyme inhibition or deficiency in ceramide metabolism. In our study, the results from the effect of FBI are consistent with those from nSMase2 deficiency, supporting the conclusion that reduction of ceramide generation leads to increase of ATP levels and, potentially, other beneficial effects, such as resistance to mitotoxic insults.

While reduction of ceramide levels is likely to be protective to mitochondria, excess ceramide elevation is common to several neurodegenerative diseases. We and others have shown that A $\beta$  activates nSMase2 and increases ceramide levels in astrocytes and other neural cells (3, 4, 96–99). It is reasonable to assume that mitotoxicity of ceramide involves a cascade of cooperating mechanisms depending on its concentration and distribution. Therefore, inhibiting ceramide biosynthesis or downregulating nSMase2 may protect mitochondria from A $\beta$ -induced damage, although definition of the exact mechanism will still require additional research. One should also keep in mind that our experiments were performed with cells in vitro. Any in vitro model can only approximate the in vivo process and is subject to experimental limitations, particularly when attempting to emulate the conditions in the aging human brain. Despite this limitation, preventing ceramide elevation emerges as a promising strategy for therapy of AD and other neurodegenerative diseases and our results will help define a common function of ceramide in the regulation and dysregulation of mitochondria in normal and pathological brain, respectively. 

The authors thank Dr. Christophe Poirier, Indiana University-Purdue University, Indianapolis, IN, for providing the nSMase2-deficient *fro/fro* mouse. They are also grateful to Dr. Mariana Nikolova-Karakashian, University of Kentucky, for critically reading the manuscript. The authors are thankful for assistance by the Augusta University imaging core facility (director Dr. Paul McNeil), particularly Dr. Anna McNeil and Tim Kurtz, for assistance with NSTORM. They thank the Department of Neuroscience and Regenerative Medicine (Chair Dr. Lin Mei) at Augusta University and the Department of Physiology (Chair Dr. Alan Daugherty) at the University of Kentucky for support.

## REFERENCES

- Kennedy, M. A., T. C. Moffat, K. Gable, S. Ganesan, K. Niewola-Staszewska, A. Johnston, C. Nislow, G. Giaever, L. J. Harris, R. Loewith, et al. 2016. A signaling lipid associated with Alzheimer's disease promotes mitochondrial dysfunction. *Sci. Rep.* **6**: 19332.
- Chakrabarti, S. S., A. Bir, J. Poddar, M. Sinha, A. Ganguly, and S. Chakrabarti. 2016. Ceramide and sphingosine-1-phosphate in cell death pathways: relevance to the pathogenesis of Alzheimer's disease. *Curr. Alzheimer Res.* **13**: 1232–1248.
- Dinkins, M. B., J. Enasko, C. Hernandez, G. Wang, J. Kong, I. Helwa, Y. Liu, A. V. Terry, Jr., and E. Bieberich. 2016. Neutral sphingomyelinase-2 deficiency ameliorates Alzheimer's disease pathology and improves cognition in the 5XFAD mouse. *J. Neurosci.* **36**: 8653–8667.
- Wang, G., M. Dinkins, Q. He, G. Zhu, C. Poirier, A. Campbell, M. Mayer-Proschel, and E. Bieberich. 2012. Astrocytes secrete exosomes enriched with proapoptotic ceramide and prostate apoptosis response 4 (PAR-4): potential mechanism of apoptosis induction in Alzheimer disease (AD). *J. Biol. Chem.* **287**: 21384–21395.
- Milhas, D., C. J. Clarke, J. Idkowiak-Baldys, D. Canals, and Y. A. Hannun. 2010. Anterograde and retrograde transport of neutral sphingomyelinase-2 between the Golgi and the plasma membrane. *Biochim. Biophys. Acta.* **1801**: 1361–1374.
- Clarke, C. J., J. M. Guthrie, and Y. A. Hannun. 2008. Regulation of neutral sphingomyelinase-2 (nSMase2) by tumor necrosis factor- $\alpha$  involves protein kinase C- $\delta$  in lung epithelial cells. *Mol. Pharmacol.* **74**: 1022–1032.
- Marchesini, N., C. Luberto, and Y. A. Hannun. 2003. Biochemical properties of mammalian neutral sphingomyelinase 2 and its role in sphingolipid metabolism. *J. Biol. Chem.* **278**: 13775–13783.
- Airola, M. V., P. Shanbhogue, A. A. Shamseddine, K. E. Guja, C. E. Senkal, R. Maini, N. Bartke, B. X. Wu, L. M. Obeid, M. Garcia-Diaz, et al. 2017. Structure of human nSMase2 reveals an interdomain allosteric activation mechanism for ceramide generation. *Proc. Natl. Acad. Sci. USA.* **114**: E5549–E5558.
- Das, A., M. S. Brown, D. D. Anderson, J. L. Goldstein, and A. Radhakrishnan. 2014. Three pools of plasma membrane cholesterol and their relation to cholesterol homeostasis. *eLife.* **3**: 02882.
- Bartke, N., and Y. A. Hannun. 2009. Bioactive sphingolipids: metabolism and function. *J. Lipid Res.* **50(Suppl)**: S91–S96.
- Bieberich, E. 2012. It's a lipid's world: bioactive lipid metabolism and signaling in neural stem cell differentiation. *Neurochem. Res.* **37**: 1208–1229.
- Futerman, A. H., and Y. A. Hannun. 2004. The complex life of simple sphingolipids. *EMBO Rep.* **5**: 777–782.
- Gault, C. R., L. M. Obeid, and Y. A. Hannun. 2010. An overview of sphingolipid metabolism: from synthesis to breakdown. *Adv. Exp. Med. Biol.* **688**: 1–23.
- Hannun, Y. A., and L. M. Obeid. 2011. Many ceramides. *J. Biol. Chem.* **286**: 27855–27862.
- Wu, B. X., C. J. Clarke, and Y. A. Hannun. 2010. Mammalian neutral sphingomyelinases: regulation and roles in cell signaling responses. *Neuromolecular Med.* **12**: 320–330.
- Zhang, Y., X. Li, K. A. Becker, and E. Gulbins. 2009. Ceramide-enriched membrane domains—structure and function. *Biochim. Biophys. Acta.* **1788**: 178–183.
- Gulbins, E., and R. Kolesnick. 2003. Raft ceramide in molecular medicine. *Oncogene.* **22**: 7070–7077.
- Burgert, A., J. Schlegel, J. Becam, S. Doose, E. Bieberich, A. Schubert-Unkmeir, and M. Sauer. 2017. Characterization of plasma membrane ceramides by super-resolution microscopy. *Angew. Chem. Int. Ed. Engl.* **56**: 6131–6135.
- Kong, J. N., K. Hardin, M. Dinkins, G. Wang, Q. He, T. Mujadzic, G. Zhu, J. Bielawski, S. Spassieva, and E. Bieberich. 2015. Regulation of Chlamydomonas flagella and ependymal cell motile cilia by ceramide-mediated translocation of GSK3. *Mol. Biol. Cell.* **26**: 4451–4465.
- He, Q., G. Wang, S. Wakade, S. Dasgupta, M. Dinkins, J. N. Kong, S. D. Spassieva, and E. Bieberich. 2014. Primary cilia in stem cells and neural progenitors are regulated by neutral sphingomyelinase 2 and ceramide. *Mol. Biol. Cell.* **25**: 1715–1729.
- He, Q., G. Wang, S. Dasgupta, M. Dinkins, G. Zhu, and E. Bieberich. 2012. Characterization of an apical ceramide-enriched compartment regulating ciliogenesis. *Mol. Biol. Cell.* **23**: 3156–3166.
- Bieberich, E. 2011. Ceramide in stem cell differentiation and embryo development: novel functions of a topological cell-signaling lipid and the concept of ceramide compartments. *J. Lipids.* **2011**: 610306.
- Wang, G., K. Krishnamurthy, and E. Bieberich. 2009. Regulation of primary cilia formation by ceramide. *J. Lipid Res.* **50**: 2103–2110.
- Krishnamurthy, K., S. Dasgupta, and E. Bieberich. 2007. Development and characterization of a novel anti-ceramide antibody. *J. Lipid Res.* **48**: 968–975.

25. Walter, T., L. Collenburg, L. Japtok, B. Kleuser, S. Schneider-Schaulies, N. Muller, J. Becam, A. Schubert-Unkmeir, J. N. Kong, E. Bieberich, et al. 2016. Incorporation and visualization of azido-functionalized N-oleoyl serinol in Jurkat cells, mouse brain astrocytes, 3T3 fibroblasts and human brain microvascular endothelial cells. *Chem. Commun. (Camb.)* **52**: 8612–8614.
26. Kong, J. N., K. Hardin, M. Dinkins, G. Wang, Q. He, T. Mujadzic, G. Zhu, J. Bielawski, S. Spassieva, and E. Bieberich. 2015. Regulation of Chlamydomonas flagella and ependymal cell motile cilia by ceramide-mediated translocation of GSK3. *Mol. Biol. Cell* **26**: 4451–4465.
27. Muscoli, C., T. Doyle, C. Dagostino, L. Bryant, Z. Chen, L. R. Watkins, J. Ryerse, E. Bieberich, W. Neumann, and D. Salvemini. 2010. Counter-regulation of opioid analgesia by glial-derived bioactive sphingolipids. *J. Neurosci.* **30**: 15400–15408.
28. Kota, V., Z. M. Szulc, and H. Hama. 2012. Identification of C(6)-ceramide-interacting proteins in D6P2T Schwannoma cells. *Proteomics* **12**: 2179–2184.
29. Elsen, L., R. Betz, G. Schwarzmann, K. Sandhoff, and G. van Echten-Deckert. 2002. Identification of ceramide binding proteins in neuronal cells: a critical point of view. *Neurochem. Res.* **27**: 717–727.
30. Wolff, J. 2009. Plasma membrane tubulin. *Biochim. Biophys. Acta* **1788**: 1415–1433.
31. Bernier-Valentin, F., D. Aunis, and B. Rousset. 1983. Evidence for tubulin-binding sites on cellular membranes: plasma membranes, mitochondrial membranes, and secretory granule membranes. *J. Cell Biol.* **97**: 209–216.
32. Rostovtseva, T. K., N. Kazemi, M. Weinrich, and S. M. Bezrukov. 2006. Voltage gating of VDAC is regulated by nonlamellar lipids of mitochondrial membranes. *J. Biol. Chem.* **281**: 37496–37506.
33. Rostovtseva, T. K., and S. M. Bezrukov. 2008. VDAC regulation: role of cytosolic proteins and mitochondrial lipids. *J. Bioenerg. Biomembr.* **40**: 163–170.
34. Rostovtseva, T. K., P. A. Gurnev, M. Y. Chen, and S. M. Bezrukov. 2012. Membrane lipid composition regulates tubulin interaction with mitochondrial voltage-dependent anion channel. *J. Biol. Chem.* **287**: 29589–29598.
35. Manczak, M., and P. H. Reddy. 2012. Abnormal interaction of VDACL1 with amyloid beta and phosphorylated tau causes mitochondrial dysfunction in Alzheimer's disease. *Hum. Mol. Genet.* **21**: 5131–5146.
36. Manczak, M., T. Sheiko, W. J. Craigen, and P. H. Reddy. 2013. Reduced VDACL1 protects against Alzheimer's disease, mitochondria, and synaptic deficiencies. *J. Alzheimers Dis.* **37**: 679–690.
37. Ben-Hail, D., R. Begas-Shvartz, M. Shalev, A. Shteiinfer-Kuzmine, A. Gruzman, S. Reina, V. De Pinto, and V. Shoshan-Barmatz. 2016. Novel compounds targeting the mitochondrial protein VDACL1 inhibit apoptosis and protect against mitochondrial dysfunction. *J. Biol. Chem.* **291**: 24986–25003.
38. Shoshan-Barmatz, V., V. De Pinto, M. Zweckstetter, Z. Raviv, N. Keinan, and N. Arbel. 2010. VDAC, a multi-functional mitochondrial protein regulating cell life and death. *Mol. Aspects Med.* **31**: 227–285.
39. Reddy, P. H. 2013. Amyloid beta-induced glycogen synthase kinase 3beta phosphorylated VDACL1 in Alzheimer's disease: implications for synaptic dysfunction and neuronal damage. *Biochim. Biophys. Acta* **1832**: 1913–1921.
40. Geisler, S., K. M. Holmstrom, D. Skujat, F. C. Fiesel, O. C. Rothfuss, P. J. Kahle, and W. Springer. 2010. PINK1/Parkin-mediated mitophagy is dependent on VDACL1 and p62/SQSTM1. *Nat. Cell Biol.* **12**: 119–131.
41. Le Verche, V., and S. Przedborski. 2010. Is amyotrophic lateral sclerosis a mitochondrial channelopathy? *Neuron* **67**: 523–524.
42. Johri, A., and M. F. Beal. 2012. Mitochondrial dysfunction in neurodegenerative diseases. *J. Pharmacol. Exp. Ther.* **342**: 619–630.
43. Camara, A. K., E. J. Lesnefsky, and D. F. Stowe. 2010. Potential therapeutic benefits of strategies directed to mitochondria. *Antioxid. Redox Signal.* **13**: 279–347.
44. Rui, Y., and J. Q. Zheng. 2016. Amyloid beta oligomers elicit mitochondrial transport defects and fragmentation in a time-dependent and pathway-specific manner. *Mol. Brain* **9**: 79.
45. Fatima, M., B. Prajapati, K. Saleem, R. Kumari, C. Mohindar Singh Singal, and P. Seth. 2017. Novel insights into role of miR-320a-VDACL1 axis in astrocyte-mediated neuronal damage in neuroAIDS. *Glia* **65**: 250–263.
46. Arif, T., L. Vasilkovsky, Y. Refaely, A. Konson, and V. Shoshan-Barmatz. 2014. Silencing VDACL1 expression by siRNA inhibits cancer cell proliferation and tumor growth in vivo. *Mol. Ther. Nucleic Acids* **3**: e159.
47. Butt, A. M. 2011. ATP: a ubiquitous gliotransmitter integrating neuron-glia networks. *Semin. Cell Dev. Biol.* **22**: 205–213.
48. Rivera, A., I. Vanzulli, and A. M. Butt. 2016. A central role for ATP signalling in glial interactions in the CNS. *Curr. Drug Targets* **17**: 1829–1833.
49. Harada, K., T. Kamiya, and T. Tsuboi. 2016. Gliotransmitter release from astrocytes: functional, developmental, and pathological implications in the brain. *Front. Neurosci.* **9**: 499.
50. Fields, R. D., and B. Stevens. 2000. ATP: an extracellular signaling molecule between neurons and glia. *Trends Neurosci.* **23**: 625–633.
51. Maldonado, E. N., and J. J. Lemasters. 2012. Warburg revisited: regulation of mitochondrial metabolism by voltage-dependent anion channels in cancer cells. *J. Pharmacol. Exp. Ther.* **342**: 637–641.
52. Maldonado, E. N., K. L. Sheldon, D. N. DeHart, J. Patnaik, Y. Manevich, D. M. Townsend, S. M. Bezrukov, T. K. Rostovtseva, and J. J. Lemasters. 2013. Voltage-dependent anion channels modulate mitochondrial metabolism in cancer cells: regulation by free tubulin and erastin. *J. Biol. Chem.* **288**: 11920–11929.
53. Maldonado, E. N. 2017. VDAC-tubulin, an anti-Warburg pro-oxidant switch. *Front. Oncol.* **7**: 4.
54. Noskov, S. Y., T. K. Rostovtseva, and S. M. Bezrukov. 2013. ATP transport through VDAC and the VDAC-tubulin complex probed by equilibrium and nonequilibrium MD simulations. *Biochemistry* **52**: 9246–9256.
55. Martel, C., Z. Wang, and C. Brenner. 2014. VDAC phosphorylation, a lipid sensor influencing the cell fate. *Mitochondrion* **19 Pt A**: 69–77.
56. Hoogerheide, D. P., S. Y. Noskov, D. Jacobs, L. Bergdoll, V. Silin, D. L. Worcester, J. Abramson, H. Nanda, T. K. Rostovtseva, and S. M. Bezrukov. 2017. Structural features and lipid binding domain of tubulin on biomimetic mitochondrial membranes. *Proc. Natl. Acad. Sci. USA* **114**: E3622–E3631.
57. Bionda, C., J. Portoukalian, D. Schmitt, C. Rodriguez-Lafrasse, and D. Ardail. 2004. Subcellular compartmentalization of ceramide metabolism: MAM (mitochondria-associated membrane) and/or mitochondria? *Biochem. J.* **382**: 527–533.
58. Hayashi, T., and M. Fujimoto. 2010. Detergent-resistant microdomains determine the localization of sigma-1 receptors to the endoplasmic reticulum-mitochondria junction. *Mol. Pharmacol.* **77**: 517–528.
59. Wu, B. X., V. Rajagopalan, P. L. Roddy, C. J. Clarke, and Y. A. Hannun. 2010. Identification and characterization of murine mitochondria-associated neutral sphingomyelinase (MA-nSMase), the mammalian sphingomyelin phosphodiesterase 5. *J. Biol. Chem.* **285**: 17993–18002.
60. Perera, M. N., V. Ganesan, L. J. Siskind, Z. M. Szulc, A. Bielawska, R. Bittman, and M. Colombini. 2016. Ceramide channel: structural basis for selective membrane targeting. *Chem. Phys. Lipids* **194**: 110–116.
61. Birbes, H., S. El Bawab, Y. A. Hannun, and L. M. Obeid. 2001. Selective hydrolysis of a mitochondrial pool of sphingomyelin induces apoptosis. *FASEB J.* **15**: 2669–2679.
62. Novgorodov, S. A., D. A. Chudakova, B. W. Wheeler, J. Bielawski, M. S. Kindy, L. M. Obeid, and T. I. Gudiz. 2011. Developmentally regulated ceramide synthase 6 increases mitochondrial Ca<sup>2+</sup> loading capacity and promotes apoptosis. *J. Biol. Chem.* **286**: 4644–4658.
63. Adler, J., and I. Parmryd. 2010. Quantifying colocalization by correlation: the Pearson correlation coefficient is superior to the Mander's overlap coefficient. *Cytometry A* **77**: 733–742.
64. Sarkar, P., I. Zaja, M. Bienengraeber, K. R. Rarick, M. Terashvili, S. Canfield, J. R. Falck, and D. R. Harder. 2014. Epoxyeicosatrienoic acids pretreatment improves amyloid beta-induced mitochondrial dysfunction in cultured rat hippocampal astrocytes. *Am. J. Physiol. Heart Circ. Physiol.* **306**: H475–H484.
65. Cowart, L. A., Z. Szulc, A. Bielawska, and Y. A. Hannun. 2002. Structural determinants of sphingolipid recognition by commercially available anti-ceramide antibodies. *J. Lipid Res.* **43**: 2042–2048.
66. Haberkant, P., and J. C. Holthuis. 2014. Fat & fabulous: bifunctional lipids in the spotlight. *Biochim. Biophys. Acta* **1841**: 1022–1030.
67. Haberkant, P., R. Rajmakers, M. Wildwater, T. Sachsenheimer, B. Brugger, K. Maeda, M. Houweling, A. C. Gavin, C. Schultz, G. van Meer, et al. 2013. In vivo profiling and visualization of cellular protein-lipid interactions using bifunctional fatty acids. *Angew. Chem. Int. Ed. Engl.* **52**: 4033–4038.

68. Haberkant, P., F. Stein, D. Hoglinger, M. J. Gerl, B. Brugger, P. P. Van Veldhoven, J. Krijgsveld, A. C. Gavin, and C. Schultz. 2016. Bifunctional sphingosine for cell-based analysis of protein-sphingolipid interactions. *ACS Chem. Biol.* **11**: 222–230.
69. Gard, D. L., and M. W. Kirschner. 1987. Microtubule assembly in cytoplasmic extracts of *Xenopus* oocytes and eggs. *J. Cell Biol.* **105**: 2191–2201.
70. Lee, J. C., and S. N. Timasheff. 1975. The reconstitution of microtubules from purified calf brain tubulin. *Biochemistry.* **14**: 5183–5187.
71. Prota, A. E., K. Bargsten, J. F. Diaz, M. Marsh, C. Cuevas, M. Liniger, C. Neuhaus, J. M. Andreu, K. H. Altmann, and M. O. Steinmetz. 2014. A new tubulin-binding site and pharmacophore for microtubule-destabilizing anticancer drugs. *Proc. Natl. Acad. Sci. USA.* **111**: 13817–13821.
72. Löwe, J., H. Li, K. H. Downing, and E. Nogales. 2001. Refined structure of alpha beta-tubulin at 3.5 Å resolution. *J. Mol. Biol.* **313**: 1045–1057.
73. Höglinger, D., A. Nadler, P. Haberkant, J. Kirkpatrick, M. Schifferer, F. Stein, S. Hauke, F. D. Porter, and C. Schultz. 2017. Trifunctional lipid probes for comprehensive studies of single lipid species in living cells. *Proc. Natl. Acad. Sci. USA.* **114**: 1566–1571.
74. Hayashi, T., R. Rizzuto, G. Hajnoczky, and T. P. Su. 2009. MAM: more than just a housekeeper. *Trends Cell Biol.* **19**: 81–88.
75. Rivero, S., J. Cardenas, M. Bornens, and R. M. Rios. 2009. Microtubule nucleation at the cis-side of the Golgi apparatus requires AKAP450 and GM130. *EMBO J.* **28**: 1016–1028.
76. Weibrecht, I., K. J. Leuchowius, C. M. Clausson, T. Conze, M. Jarvius, W. M. Howell, M. Kamali-Moghaddam, and O. Soderberg. 2010. Proximity ligation assays: a recent addition to the proteomics toolbox. *Expert Rev. Proteomics.* **7**: 401–409.
77. Gullberg, M., S. Fredriksson, M. Taussig, J. Jarvius, S. Gustafsdottir, and U. Landegren. 2003. A sense of closeness: protein detection by proximity ligation. *Curr. Opin. Biotechnol.* **14**: 82–86.
78. Rostovtseva, T. K., K. L. Sheldon, E. Hassanzadeh, C. Monge, V. Saks, S. M. Bezrukov, and D. L. Sackett. 2008. Tubulin binding blocks mitochondrial voltage-dependent anion channel and regulates respiration. *Proc. Natl. Acad. Sci. USA.* **105**: 18746–18751.
79. Roundhill, E., D. Turnbull, and S. Burchill. 2016. Localization of MRP-1 to the outer mitochondrial membrane by the chaperone protein HSP90beta. *FASEB J.* **30**: 1712–1723.
80. Lahiri, S., and A. H. Futerman. 2005. LASS5 is a bona fide dihydroceramide synthase that selectively utilizes palmitoyl-CoA as acyl donor. *J. Biol. Chem.* **280**: 33735–33738.
81. Hoppel, C., and C. Cooper. 1968. The action of digitonin on rat liver mitochondria. The effects on enzyme content. *Biochem. J.* **107**: 367–375.
82. Abu-Hamad, S., S. Sivan, and V. Shoshan-Barmatz. 2006. The expression level of the voltage-dependent anion channel controls life and death of the cell. *Proc. Natl. Acad. Sci. USA.* **103**: 5787–5792.
83. Hou, Q., J. Jin, H. Zhou, S. A. Novgorodov, A. Bielawska, Z. M. Szulc, Y. A. Hannun, L. M. Obeid, and Y. T. Hsu. 2011. Mitochondrially targeted ceramides preferentially promote autophagy, retard cell growth, and induce apoptosis. *J. Lipid Res.* **52**: 278–288.
84. Siskind, L. J., R. N. Kolesnick, and M. Colombini. 2002. Ceramide channels increase the permeability of the mitochondrial outer membrane to small proteins. *J. Biol. Chem.* **277**: 26796–26803.
85. Siskind, L. J., L. Feinstein, T. Yu, J. S. Davis, D. Jones, J. Choi, J. E. Zuckerman, W. Tan, R. B. Hill, J. M. Hardwick, et al. 2008. Anti-apoptotic Bcl-2 family proteins disassemble ceramide channels. *J. Biol. Chem.* **283**: 6622–6630.
86. Haberkant, P., and G. van Meer. 2009. Protein-lipid interactions: paparazzi hunting for snap-shots. *Biol. Chem.* **390**: 795–803.
87. Doczi, J., B. Torocsik, A. Echaniz-Laguna, B. Mousson de Camaret, A. Starkov, N. Starkova, A. Gal, M. J. Molnar, H. Kawamata, G. Manfredi, et al. 2016. Alterations in voltage-sensing of the mitochondrial permeability transition pore in ANT1-deficient cells. *Sci. Rep.* **6**: 26700.
88. Dany, M., and B. Ogretmen. 2015. Ceramide induced mitophagy and tumor suppression. *Biochim. Biophys. Acta.* **1853**: 2834–2845.
89. Law, B. A., X. Liao, K. S. Moore, A. Southard, P. Roddy, R. Ji, Z. Sulz, A. Bielawska, P. C. Schulze, and L. A. Cowart. Lipotoxic very-long-chain ceramides cause mitochondrial dysfunction, oxidative stress, and cell death in cardiomyocytes. *FASEB J.* Epub ahead of print. November 10, 2017; doi:10.1096/fj.201700300R.
90. Beck, H., K. Flynn, K. S. Lindenberg, H. Schwarz, F. Bradke, S. Di Giovanni, and B. Knoll. 2012. Serum response factor (SRF)-cofilin-actin signaling axis modulates mitochondrial dynamics. *Proc. Natl. Acad. Sci. USA.* **109**: E2523–E2532.
91. Kremneva, E., M. Kislin, X. Kang, and L. Khiroug. 2013. Motility of astrocytic mitochondria is arrested by Ca<sup>2+</sup>-dependent interaction between mitochondria and actin filaments. *Cell Calcium.* **53**: 85–93.
92. Chen, Y., S. Han, X. Huang, J. Ni, and X. He. 2016. The protective effect of icariin on mitochondrial transport and distribution in primary hippocampal neurons from 3× Tg-AD mice. *Int. J. Mol. Sci.* **17**: E163.
93. Domijan, A. M., and A. Y. Abramov. 2011. Fumonisin B1 inhibits mitochondrial respiration and deregulates calcium homeostasis—implication to mechanism of cell toxicity. *Int. J. Biochem. Cell Biol.* **43**: 897–904.
94. Lee, H., J. A. Rotolo, J. Mesicek, T. Penate-Medina, A. Rimner, W. C. Liao, X. Yin, G. Ragupathi, D. Ehleiter, E. Gulbins, et al. 2011. Mitochondrial ceramide-rich macrodomains functionalize Bax upon irradiation. *PLoS One.* **6**: e19783.
95. Kroesen, B. J., B. Pettus, C. Luberto, M. Busman, H. Sietsma, L. de Leij, and Y. A. Hannun. 2001. Induction of apoptosis through B-cell receptor cross-linking occurs via de novo generated C16-ceramide and involves mitochondria. *J. Biol. Chem.* **276**: 13606–13614.
96. Jana, A., and K. Pahan. 2010. Fibrillar amyloid-beta-activated human astroglia kill primary human neurons via neutral sphingomyelinase: implications for Alzheimer's disease. *J. Neurosci.* **30**: 12676–12689.
97. Haughey, N. J., V. V. Bandaru, M. Bae, and M. P. Mattson. 2010. Roles for dysfunctional sphingolipid metabolism in Alzheimer's disease neuropathogenesis. *Biochim. Biophys. Acta.* **1801**: 878–886.
98. Zeng, C., J. T. Lee, H. Chen, S. Chen, C. Y. Hsu, and J. Xu. 2005. Amyloid-beta peptide enhances tumor necrosis factor-alpha-induced iNOS through neutral sphingomyelinase/ceramide pathway in oligodendrocytes. *J. Neurochem.* **94**: 703–712.
99. Yang, D. I., C. H. Yeh, S. Chen, J. Xu, and C. Y. Hsu. 2004. Neutral sphingomyelinase activation in endothelial and glial cell death induced by amyloid beta-peptide. *Neurobiol. Dis.* **17**: 99–107.